Journal of Atmospheric and Solar–Terrestrial Physics 162 (2017) 136–150

Contents lists available at ScienceDirect

Journal of Atmospheric and Solar–Terrestrial Physics

journal homepage: www.elsevier.com/locate/jastp

Sensitivity of equatorial atomic oxygen in the MLT region to the 11-year and 27-day solar cycles

Olexandr Lednyts'kyy[a,*], Christian von Savigny[a], Mark Weber[b]

[a] Institute of Physics, Ernst-Moritz-Arndt-University of Greifswald, 17489 Greifswald, Germany
[b] Institute of Environmental Physics, University of Bremen, 28334 Bremen, Germany

ARTICLE INFO

Keywords:
Nightglow
Green line emission
O(1S-1D)
Atomic oxygen
O(3P)
O(1S)
Remote sensing

ABSTRACT

We report on 27-day and 11-year solar cycle signatures in atomic oxygen (O) concentrations ([O]) in the MLT (Mesosphere/Lower Thermosphere) region of the terrestrial atmosphere. MLT [O] profiles were retrieved on the base of green line (557.7 nm) nightglow data sets provided by the SCanning Imaging Absorption spectroMeter for Atmospheric CHartographY (SCIAMACHY) onboard Envisat from 2002 to 2012. A statistically significant solar 27-day signature was identified (and then quantified with respect to the sensitivity and phase relationship to solar forcing) in time series of MLT [O] profiles with use of cross-correlation and superposed epoch analysis techniques. It was the first identification of the solar 27-day signature in MLT atomic oxygen on the base of such experimental data sets. The sensitivity of [O] to solar cycle variability at the 11-year time scale was quantified with use of cross-correlation and multiple-linear regression analysis techniques, which yield results consistent with known studies and, particularly, indicate that the sensitivity of [O] to solar forcing increases with increasing altitude. A comparison of obtained values of atomic oxygen sensitivity in response to solar forcing at the 27-day and 11-year time scales reveals the fact that the sensitivities agree well to each other within their uncertainties during the descending phase of the last (23rd) 11-year cycle of solar activity, whereas the [O] sensitivity values at the 27-day time scale during the last solar minimum phase were lower than those ones during the descending phase. It was also determined that atomic oxygen is in-phase with the solar forcing (in agreement with model results) at the 11-year time scale, whereas the time lag of the 27-day signature in response to solar forcing was about 12 – 14 days.

1. Introduction

Atomic oxygen (O) is one of the most important chemical constituents in the MLT (Mesosphere/Lower Thermosphere) region of the terrestrial atmosphere. Being chemically directly coupled to ozone (O_3), atomic oxygen is – due to its long lifetime – an important carrier of chemical potential energy and it causes radiative cooling at 63 μm in the upper mesosphere (Beig et al., 2008). Atomic oxygen is also of crucial importance, because it drives airglow emissions (by $O(^1S - ^1D)$, OH* and O_2^*) frequently used to remotely sense the Earth's upper atmosphere.

Variations of solar spectral irradiance at the 11-year and 27-day time scales (McIntosh et al., 2015) are known to affect many atmospheric minor parameters. There are numerous model studies that consider 11-year (e.g., Schmidt et al., 2006; Marsh et al., 2007) and 27-day (e.g., Gruzdev et al., 2009) solar cycle effects on the composition of the atmosphere in the MLT region. However, the number of corresponding studies based on observations is quite limited. In terms of 27-day solar cycle effects there are studies concerning noctilucent clouds (NLCs) (e.g., Robert et al., 2010; von Savigny et al., 2013), stratospheric and mesospheric O_3 (e.g., Hood, 1986; Fioletov, 2009), temperature (e.g., Hood, 1986; von Savigny et al., 2012; Thomas et al., 2015) and water (e.g., Thomas et al., 2015). There are also several studies addressing 11-year solar cycle signatures identified in atomic oxygen data sets provided by satellites (Russell et al., 2004; Kaufmann et al., 2014; Lednyts'kyy et al., 2015; Zhu et al., 2015).

The aim of the present research is to quantify the solar 11-year and 27-day signatures in MLT atomic oxygen profiles retrieved from nighttime oxygen greenline measurements with SCIAMACHY on the Envisat spacecraft. First, we provide a brief overview of the existing studies on 11-year and 27-day solar cycle signatures in atomic oxygen in the MLT region.

Russell et al. (2004) retrieved atomic oxygen concentration profiles in the MLT region from Wind Imaging Interferometer (WINDII) observations on board the Upper Atmosphere Research Satellite (UARS). They identified a dependence of [O] on solar activity at altitudes above about 96 km.

* Corresponding author.
E-mail address: olexandr.lednytskyy@uni-greifswald.de (O. Lednyts'kyy).

http://dx.doi.org/10.1016/j.jastp.2016.11.003
Received 22 February 2016; Received in revised form 12 September 2016; Accepted 12 November 2016
Available online 19 November 2016

Model simulations of the atmospheric response to changes in solar forcing over the 11-year solar cycle were, e.g., performed with the Whole Atmosphere Community Climate Model, version 3 (WACCM3) (Marsh et al., 2007) and with the Hamburg Model of the Neutral and Ionized Atmosphere (HAMMONIA) (Schmidt et al., 2006). The general circulation model WACCM3 used by Marsh et al. (2007) incorporates interactive chemistry of both neutral and ion species exposed to solar radiation and energetic particles. The modeled relative change in July mean atomic oxygen volume mixing ratio between the solar maximum and minimum is slightly larger than 20% in the 90 – 100 km altitude range and for latitudes between 0° and 20 °N (see Fig. 12d in Marsh et al., 2007). The chemistry-climate model HAMMONIA used by Schmidt et al. (2006) considers relevant radiative and dynamical processes coupled to a chemistry module containing 48 compounds. The model results show a relative change of zonal mean July atomic oxygen volume mixing ratio for the solar maximum relative to the solar minimum conditions of slightly less than 20% in the 90–100 km altitude range and in the latitude range 0 ° – 20 °N (see Fig. 12e in Schmidt et al., 2006).

Liu and Shepherd (2008) found that O(^{1}S) nightglow volume emission rates (VER) retrieved from WINDII/UARS observations increase linearly with increasing solar F10.7 cm flux. Moreover, the solar influence on the O(^{1}S) nightglow appears to be modulated by seasonal variations, and Liu and Shepherd (2008) derived an empirical formula to predict three-month averages of the vertically integrated O(^{1}S) emission rates using the F10.7 flux data and some coefficients describing linear and seasonal variations of the O(^{1}S) emission rates.

In a very recent study, Kaufmann et al. (2014) retrieved – similar to Lednyts'kyy et al. (2015) and von Savigny and Lednyts'kyy (2013) – MLT atomic oxygen profiles from monthly averaged SCIAMACHY O greenline observations based on the well-known cubic equation (McDade et al., 1986). Kaufmann et al. (2014) found annual mean [O] changes between the solar maximum and minimum of 5% at 90 km and 25% at 102 km, with [O] being in phase with the F10.7 solar flux.

The number of available studies on the solar 27-day response of atomic oxygen in the MLT is very limited and restricted to model simulations.

Gruzdev et al. (2009) used HAMMONIA model simulations to investigate the response of middle atmosphere chemical composition – including atomic oxygen – to the 27-day solar forcing. The model results show that the O(^3P) sensitivity decreases with increasing altitude in the 80 – 120 km altitude range.

The phase characteristics of the O(^3P) response to the 27-day solar forcing were obtained by Gruzdev et al. (2009) from phase spectra for the simulation with a three times amplified 27-day solar forcing. The modeled O(^3P) response lags the solar forcing by 4.5–7 days in the altitude range 90–100 km and in the latitude range 0° – 20 °N (see Fig. 11c in Gruzdev et al. (2009)), and is approximately in opposite phase with the O_2 response.

The paper is structured as follows. Section 2 provides a brief description of the SCIAMACHY instrument aboard Envisat. Section 3 gives an overview of the data sets used in this study. Results on the 11-year and 27-day solar cycle signatures in MLT atomic oxygen are presented in Section 4. The study employs different analysis techniques, including cross-correlation analysis, wavelet analysis and multiple-linear regression. Conclusions are provided in Section 5.

2. Brief instrumental description

SCIAMACHY (Bovensmann et al., 1999) was an 8-channel grating spectrometer on board of the European Space Agency's Envisat spacecraft that carried out atmospheric observations in nadir, limb and solar/lunar occultation geometry in the 220–2380 nm spectral range. SCIAMACHY also performed nighttime limb emission measurements in a mesosphere/thermosphere mode in the tangent height range 75–150 km. Envisat was launched on March 1st, 2002, into a polar sun-synchronous orbit with a 10:00 a.m. descending node. SCIAMACHY routine operations started on August 2nd, 2002, and ended because of an abrupt failure of the Envisat spacecraft on April 8th, 2012. For the present study we used low latitude nighttime limb measurements carried out at approximately 22:00 local solar time. SCIAMACHY nighttime limb observations are only available throughout the year for latitudes between the equator and about 25 °N. For this reason, the focus of the present study is on the latitude range 0° – 20 °N.

3. Data sets

3.1. Proxy indicators of solar activity

In the present study we employ two different solar proxy variables to characterize solar activity, i.e. the MgII index and the Lyman-α flux. Additionally we use the F10.7 cm radio flux to convert the calculated [O] sensitivity values (with respect to MgII-index and Lyman-α, see Section 4.3 and Section 4.4 for further details) to the [O] sensitivity values with respect to the F10.7-cm radio flux.

The MgII index is a dimensionless proxy of solar activity and is defined as the core-to-wing ratio of the Mg^+ Fraunhofer line at 280 nm. Near the center of the Fraunhofer line a chromospheric emission doublet occurs, which is associated with more intense emissions during periods of enhanced solar activity. Dudok de Wit et al. (2009) compared the performance of different solar proxies in terms of representing the actual solar spectral variability in different spectral regions, and found that of the studied proxies the MgII index showed the best overall performance. In this study we use a composite MgII index time series (version 4 provided by IEPUB (2015) since June 10, 2015) based on daily solar spectrum observations (Weber et al., 2013; Snow et al., 2014) with a number of different satellite instruments including SBUV(/2), GOME, SCIAMACHY and GOME-2.

The irradiance near 280 nm, where the MgII lines occur, is primarily absorbed in the O_3 Hartley band in the stratosphere through photodissociation leading to the formation of O(^{1}D). The solar irradiance in the wavelength range 122–200 nm in the far-ultraviolet region (FUV) affects the concentration of molecular oxygen and nitric oxide in the MLT region and is absorbed in the ionosphere.

The Lyman-α line is a proxy of solar activity measured in photon $cm^{-2}\ s^{-1}$. The solar irradiance at 121.6 nm is absorbed by O_2 in the mesosphere and is not absorbed by O_3 (Brasseur and Solomon, 2005). The extreme ultraviolet region (EUV) in the wavelength range 10–120 nm affects thermospheric O. In this study we also use a Lyman-α time series (version 3 provided by LISIRD (2015) since January 23, 2015) based on measurements from multiple instruments and models, whereas values of the time series are all scaled to match the UARS reference level (Woods et al., 2000).

The radio flux emitted at 10.7 cm (F10.7) or 2800 MHz has no direct impact on climate (Dukok de Wit and Watermann, 2010), but this proxy of solar activity is one of the most widely used solar proxies and is measured in units of 10^{-22} W m^{-1} Hz^{-1}, which is usually referred to as one solar flux unit (1 sfu). In this study we also use a F10.7 (Tapping, 2013) time series (version 1994.v2 available at NOAA (2015)) based on observations made by the Dominion Radio Astrophysical Observatory (Canada) at 17:00 UT daily.

3.2. Atomic oxygen concentration profiles in the MLT

The atomic oxygen concentration profiles used in this study were retrieved from O green line nightglow observations with SCIAMACHY. First, we retrieved O green line vertical volume emission rate (VER) profiles from limb emission rate (LER) profiles, using regularized total least squares minimization in the inversion procedure as described in detail by Lednyts'kyy et al. (2015). LER profiles were calculated from SCIAMACHY nighttime limb emission measurements of the oxygen 557.7 nm green line emission in five degree latitude bins with daily

time resolution and on a one km altitude grid.

To retrieve [O] profiles from O green line VER profiles we used two different photochemical schemes both based on the two-step Barth transfer scheme, as described in detail by Lednyts'kyy et al. (2015). First, the well-known cubic equation (McDade et al., 1986) was used with coefficients as discussed by Lednyts'kyy et al. (2015), taking into account SABER as a source of temperature and atmospheric pressure to calculate density profiles. Second, an extended cubic equation (Gobbi et al., 1992; Semenov, 1997) with corresponding coefficients (Lednyts'kyy et al., 2015) was used to include processes of $O(^1S)$ quenching by chemical constituents not considered in the well-known cubic equation. Note that the Energy Transfer in the Oxygen Nightglow (ETON) rocket campaign (McDade et al., 1986) was conducted in March 1982 during the maximum of the 21st solar cycle to derive the well-known cubic equation. However, the coefficients used by Lednyts'kyy et al. (2015) were adopted from studies relevant for different phases of solar activity to solve the well-known cubic equation and the extended cubic equation.

Both equations are based on the 2-step Barth transfer scheme, represented by chemical reactions accompanied by quenching. The quenching of O_2^* as well as the quenching of $O(^1S)$ by O_2 is considered in the well-known cubic equation. The quenching of $O(^1S)$ by other chemical species, e.g. $O(^3P)$ and N_2, is considered in the extended cubic equation. We consider these two cases of quenching in the following equation:

$$VER = \kappa_1[O]^2([N_2] + [O_2]) \cdot \frac{[O]}{C(0) + C(1)[O] + C(2)[O_2]} \cdot \frac{A_{558}}{A_{1S} + \sum_i ({}^i\kappa_5[M_i])} \quad (1)$$

with VER being volume emission rates (photon $cm^{-3}\ s^{-1}$), A_{558} (s^{-1}) the transition probability of $O(^1S - {}^1D)$, $A_{1S}(s^{-1})$ the inverse radiative lifetime of $O(^1S)$, the dimensionless variables $C(0)$, $C(1)$ and $C(2)$ are the empirical $O(^1S)$ excitation parameters, $\kappa_1(cm^3\ s^{-1})$ the rate coefficient for the three body recombination of atomic oxygen, ${}^i\kappa_5(\ cm^3\ s^{-1})$ the rate coefficient for quenching of $O(^1S)$ by M_i, $i = 1, 2, 3$, $[M_i] = ([O], [N_2], [O_2])$ being concentrations of atomic oxygen (i=1), molecular nitrogen (i=2) and molecular oxygen (i=3). Eq. (1) corresponds to the extended cubic equation if ${}^i\kappa_5 \neq 0$ for $i = 1, 2, 3$ and to the well-known cubic equation if ${}^1\kappa_5 = 0$ and ${}^2\kappa_5 = 0$. Lednyts'kyy et al. (2015) applied a numerical approximation to find the solution of the extended cubic equation that considers the case of the enhanced quenching and apply Eq. (1) in the time interval of SCIAMACHY observations. The state-of-the-art numerical values of the photochemical model parameters relevant for the retrieval of atomic oxygen profiles are discussed by Lednyts'kyy et al. (2015).

The sensitivity of atomic oxygen to solar forcing is a relative quantity, suggesting that the choice of the photochemical model (according to the well-known cubic equation or the extended cubic equation) should not influence the obtained sensitivity values too much. In the following we demonstrate that the sensitivities are more or less independent of the photochemical scheme chosen. For this reason, the results presented in the main part of the paper are based on the well-known cubic equation only. The SCIAMACHY atomic oxygen retrievals were also used in a recent study on quenching of vibrationally excited OH* by atomic oxygen (von Savigny and Lednyts'kyy, 2013).

To study the altitude dependent [O] sensitivity to solar forcing we used the [O] time series retrieved according to the procedure given by Lednyts'kyy et al. (2015), which takes into account data quality reports and data anomaly reports concerning SCIAMACHY operations. LER profiles used in the [O] retrieval were obtained from SCIAMACHY observations and averaged daily over longitude at a fixed local solar time of 22:00. We expect that the vertical motion field at 22:00 local time (LT) will influence limb emission rates observed by SCIAMACHY since atomic oxygen has a large vertical gradient in the MLT region. The [O] data for the entire time interval (from January 1, 2003, to December 31, 2011) were averaged in the altitude range 90–100 km as well as other altitude ranges noted explicitly hereafter (i.e., 88–90 km, 91–93 km, 94–96 km, 97–99 km, 100–102 km) as follows. The [O] and VER data were averaged daily if the corresponding VER values were higher than 1 photon $s^{-1}\ cm^{-3}$ for each altitude and latitude bin, and only for days, for which data are available in every year between 2003 and 2011. So, the same days are omitted when forming annual means for individual years. This was done in order to avoid spurious trends or solar cycle effects caused by an inhomogeneous distribution of data gaps throughout the SCIAMACHY mission period. The resulting [O] and VER time series were averaged daily in the latitude range 0° – 20 °N . Then the resulting [O] and VER time series were averaged monthly and, finally, annually.

The above mentioned criteria for rejecting days of measurements enabled us to compare the averaged data for each month or year and to perform the sensitivity analysis. The daily averaged [O] time series contains the following data gaps with a duration of more than 5 days: two gaps of 6 days each, one gap of 12 days, two gaps of 17 days each, one gap of 18 days, one gap of 20 days and one gap of 56 days. The monthly averaged [O] time series contains only one data gap and its duration is 1 month (June 2003). We read the data (with zero values in the data gaps) in and applied interpolation over the data to fill small data gaps in. In order to deal with data gaps and also to investigate potential temporal variations in the sensitivity of [O] to the 27-day solar forcing, different time intervals were defined for the analysis. The time intervals were also chosen to represent different phases of the 11-year solar cycle (McIntosh et al., 2014).

SCIAMACHY routine observations only commenced in Fall 2002, i.e., they do not cover the solar maximum 1999 – 2003. However, the descending phase of solar cycle 23 and the prolonged solar minimum are well covered. In order to study possible non-linearities in the atmospheric response to solar forcing we performed the analysis for the following time intervals:

1. the *descending-phase time interval* (for days 800 – 1500 relative to January 1, 2003, corresponding to 03/2005 – 02/2007) covering the descending phase of solar activity,
2. the *minimum-phase time interval* (for days 1500 – 2140 corresponding to 02/2007 – 11/2008) covering the solar minimum phase,
3. the *long time interval* (for days 800 – 3280 corresponding to 03/2005 – 12/2011) covering the descending, minimum and ascending phases of solar activity, and
4. the *entire time interval* (for days 1 – 3285 corresponding to 01/2003 – 12/2011), covering nine complete years of data.

4. Results and discussion

The 11-year solar cycle and the 27-day rotational solar cycle constitute the dominant periodicities in solar spectral irradiance (Dukok de Wit and Watermann, 2010). The analysis techniques used and the resulting estimates of the sensitivity of atomic oxygen to solar activity at the 11-year and 27-day time scales are described in the following.

4.1. The 11-year solar cycle signature

The phases of the 11-year solar cycle can be recognized by sight in the MgII index data set shown in the upper panel of Fig. 1. The panel displays the MgII index time series with daily (red solid line) and annual resolution (red circles) for the entire time interval (from 01/2003 to 12/2011). The equatorial [O] time series averaged over the 90 – 100 km altitude range (see Section 3.2) is shown in the lower panel of Fig. 1 with daily (small blue dots) and annual resolution (large blue circles). Annual averaging of the [O] and MgII index time series is

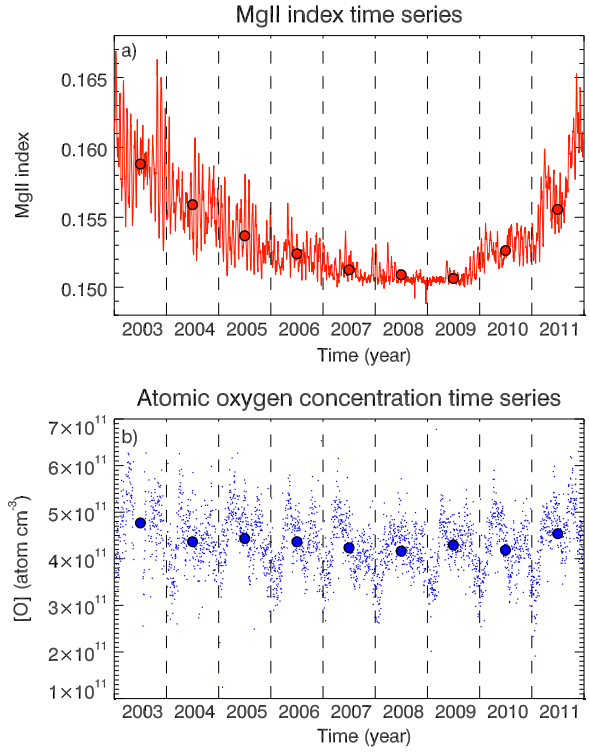

Fig. 1. Upper panel: The MgII time series with daily resolution (red line) and annually averaged (red circles). Lower panel: The [O] time series with daily resolution (small blue dots) and annually averaged (large blue circles) in the 0° – 20 °N latitude range and the 90–100 km altitude range. See Section 4.1 for further details. (For interpretation of the references to color in this figure legend, the reader is referred to the web version of this article.)

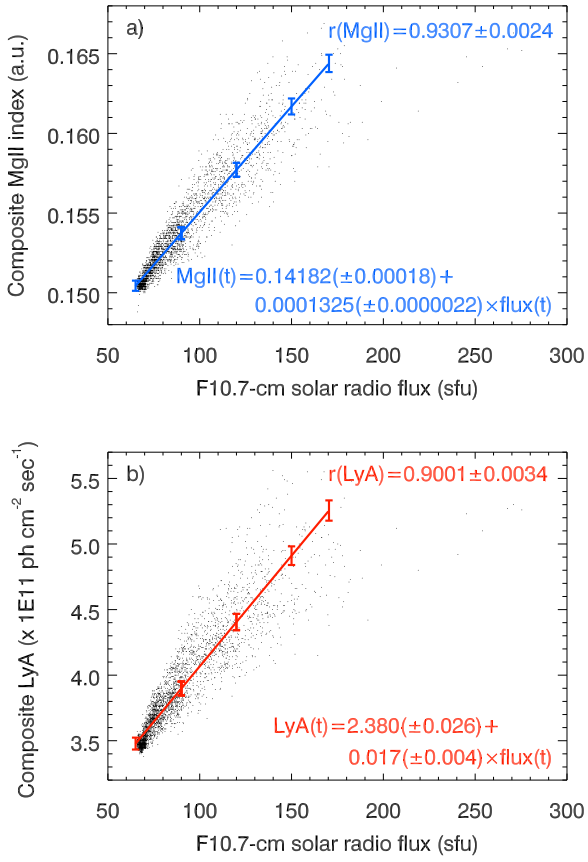

Fig. 2. Upper panel: Scatter plot of daily MgII index and F10.7 solar proxy values. The correlation coefficient and the time dependent linear regression equation are shown as well. Lower panel: similar to upper panel, but for Lyman-α. See Section 4.2 for further details. (For interpretation of the references to color in this gure legend,the reader is referred to the web version of this article.)

performed to suppress variations at time scales shorter than one year and to study the impact of solar forcing on the [O] profiles in the MLT region at the 11-year time scale. Annually averaged time series are denoted by [O^a], MgII^a, and daily averaged time series are denoted by [O^d], MgII^d.

The upper panel of Fig. 1 demonstrates that minimal MgII index values occur in the time interval from the second half of 2007 to the end of 2009, so that the chosen minimum-phase time interval (introduced in Section 3.2) is appropriate to reflect the solar minimum phase. It is difficult to determine the minimum-phase time interval with help of the [O] time series with daily resolution shown with small blue dots in the lower panel of the figure. The annually averaged [O] time series shown with large blue circles exhibits a bit longer time interval with minimal [O] values than that of minimal MgII index values. However, we analyze the [O] time series in the same time intervals defined in Section 3.2. We discuss the cross-correlation between the MgII index and the [O] anomaly data sets with daily resolution in different time intervals to address this issue in Section 4.2.3. The high solar activity during 2003 and 2004 can be recognized due to high values in the MgII index data set, but is not so obvious for [O]. The descending phase of solar activity (the descending-phase time interval introduced in Section 3.2) was chosen to study the impact of solar forcing on atomic oxygen in the MLT region at the 27-day time scale.

4.2. Quantitative estimation of the 27-day solar cycle signature

The first step applied to quantify the solar 27-day signature in MLT atomic oxygen consists of the determination of anomaly time series based on the original [O] time series with daily resolution. The anomaly time series were obtained through removal of a 35-day running mean (following earlier works by Hood (1986) and Robert et al. (2010)) followed by smoothing with a 7-day running mean. The applied smoothing technique is equivalent to the bandpass filtering (7–35 days) to suppress variations at shorter and longer time scales. Particularly, the bandpass filtering by consecutive smoothing removes non-stationarity at temporal scales larger than 35 days, which is typically present in the analyzed time series.

The impact of solar forcing on atomic oxygen in the MLT region at the 27-day time scale was determined using both the MgII and the Lyman-α solar proxies. To convert these proxy values to the F10.7 cm radio flux measured in sfu (see Section 3.1) we correlated them to the F10.7 cm radio flux (see upper and lower panels of Fig. 2) and performed a linear ordinary least squares bisector regression (Isobe et al., 1990). The linear regression line (see blue line) and corresponding uncertainties were calculated for the daily averaged values (see black dots) of the F10.7 cm radio flux and the MgII index data sets for the period 2003 – 2011 as shown in the upper panel of Fig. 2. The cross-correlation coefficient between MgII and F10.7 cm is 0.93. We also found a high correlation coefficient of 0.90 between the F10.7 cm radio flux and the Lyman-α data set. The corresponding equations of the linear relationships are displayed in blue (upper panel) and red (lower panel). Due to high values of correlation coefficients we can use the linear relationships to convert the calculated [O] sensitivity values (with respect to Lyman-α and MgII index, see Section 4.3 and Section 4.4 for further details) to the [O] sensitivity values with respect to the F10.7-cm radio flux. Finally, we can compare the converted [O] sensitivity values with studies that use F10.7 as the proxy indicator of solar activity.

In following subsections we discuss frequency spectra, time resolved spectra, phase shift resolved diagrams of the analyzed [O], MgII and Lyman-α data sets.

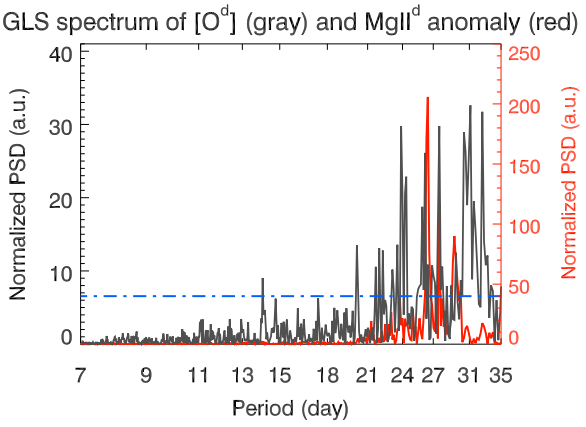

Fig. 3. Normalized power spectral density (PSD) in the generalized Lomb-Scargle (GLS) spectrum of the [O^d] anomaly time series (see gray line) and MgII^d anomaly time series (see red line). The anomaly time series were averaged daily in the entire time interval from January 2003 to December 2011 (days 1–3285). See Section 4.2.1 for further details. (For interpretation of the references to color in this figure legend, the reader is referred to the web version of this article.)

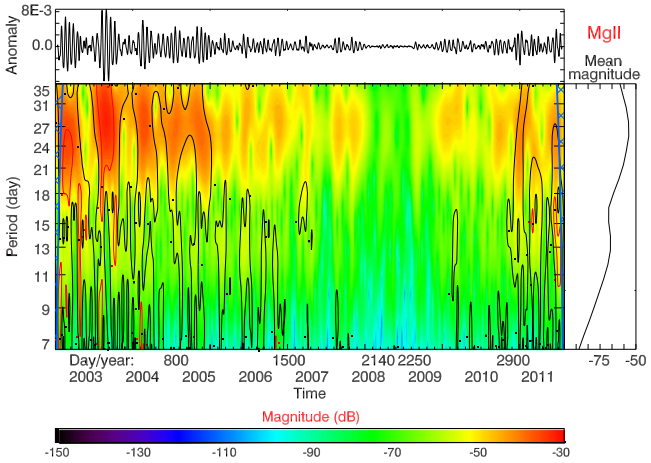

Fig. 4. The MgII index anomaly time series in the entire time interval is shown in the upper panel, the corresponding wavelet power spectrum is shown in the main part of the figure and the mean magnitude of the spectrum is shown in the right part of the figure. The cone of influence region is marked with solid lines colored in blue. The red contour line corresponds to the 99% confidence level and the black line to 68%. See Section 4.2.2 for further details. The horizontal axis includes the day numbering starting on January 1, 2003. (For interpretation of the references to color in this figure legend, the reader is referred to the web version of this article.)

4.2.1. Spectral analyses

The generalized Lomb-Scargle (GLS) method is based on a least squares fit of sinusoidal, cosinusoidal and offset components of a time series and enables to estimate a frequency spectrum of unevenly sampled data (Zechmeister and Kürster, 2009) including data uncertainties. Using the GLS method we calculated the normalized power spectral density of the zonally and daily averaged [O] ([O^d]) anomaly time series over the entire time interval. SCIAMACHY performed nighttime limb-emission observations from a sun-synchronous orbit at a fixed local solar time of 22:00. Full longitudinal geographical coverage was obtained within 3 days at the equator, and we average daily measurements zonally in 5° latitude bins (Lednyts'kyy et al., 2015). Some interruptions in the communication link to Envisat resulted in a small number of non-periodic data gaps (see Section 3.2 for details) in the latitude range 0° – 20 °N studied here.

Fig. 3 shows the GLS spectrum of the [O^d] anomaly time series (gray line), the corresponding 68% confidence (Press et al., 1997) level (blue dash-dotted line) and the GLS spectrum of the MgII^d anomaly time series (red line). The GLS-spectrum indicates a group of peaks with a periodicity of about 27 days (significant at the 68% confidence level). GLS spectra of both the [O^d] and MgII^d anomaly show rather narrow peaks at about 27, 28 and 30 days significant at the 68% confidence level. However, the GLS spectrum of the [O^d] anomaly also shows wide peaks at about 24, 31 and 32 days.

The physical-chemical drivers of the quasi-27-day signatures are not well understood - and may differ between different altitudes and latitudes. The effects may be dominated by photochemistry, i.e. photolysis and variable diabatic heating, or by dynamical processes (variable up/downwelling leading to adiabatic cooling/heating). For instance, a strong quasi-27-day oscillation (observed by Huang et al. (2015) in temperature, zonal and meridional winds) propagates from the troposphere to the MLT and reaches about 20 m/s at 90 km. This oscillation is of Rossby wave type. Huang et al. (2015) noted that the 27-day periodicity in the solar F10.7 cm radio flux is almost in phase with the reported oscillation at 90 km from December 2004 to March 2005.

It is unlikely that our results based on cross-correlation and the superposed epoch analysis are strongly affected by such oscillations. First, because our analysis is based on zonally averaged data, i.e. most of the planetary wave signatures should cancel out. Second, planetary waves are not expected to have a fixed phase relationship with solar activity, i.e. its impact should also cancel out in cross-correlation or superposed epoch analyses, if the time series is sufficiently long.

4.2.2. Time resolved spectral analysis – wavelet analysis

The generalized Lomb-Scargle method applied in the previous section does not allow investigating temporal variations of the power spectrum. To overcome this limitation we applied the wavelet analysis technique described by Torrence and Webster (1999) to the entire anomaly time series to decompose the time series into time-frequency space. The anomaly time series was convolved with a "Morlet" wavelet function. The convolution procedure is corrupted near the edges of the data set. The region of the wavelet spectrum where these edge effects can not be neglected is shown as the cone of influence (COI) (Torrence and Webster, 1999). The natural logarithm of the wavelet power was multiplied by ten to represent the resulting wavelet power spectra in decibel (dB) units. The mean magnitude of the resulting wavelet power was calculated by temporal averaging of the wavelet power spectra within the COI region.

Fig. 4 shows the MgII index anomaly time series (upper panel) in the entire time interval, the corresponding wavelet power spectrum (main part of the figure) and the mean magnitude of the spectrum (right part of the figure). We calculated the wavelet power spectrum and the corresponding confidence level, using a regular χ^2-test (Torrence and Webster, 1999). The colored contour lines shown in the contour plot reflect certain confidence levels. The red contour line corresponds to the 99% confidence level and the black line to the 68% confidence level. The COI region is marked with a solid blue line and is only visible at the left and right edges of the contour plot. The MgII index wavelet spectrum clearly shows the presence of the major 27-day periodicity in the time interval corresponding to the solar maximum phase and other minor periodicities (significant at the 95% confidence level) in the range 13–24 days during the descending and ascending phases of solar activity. High values of the wavelet power are distributed in the range 20–33 days during the entire time interval, except during the solar minimum. The mean magnitude of the spectrum exhibits the major 27-day periodicity. The wavelet spectrum of the Lyman-α time series (not shown) exhibits similar periodicities as those ones found for the MgII index.

Fig. 5 shows the [O] anomaly time series (upper panel), the corresponding wavelet power spectrum (main part of the figure), the mean magnitude of the spectrum (right part of the figure) and the COI region marked in blue. We used the same colors to mark confidence levels of the [O] wavelet spectrum as for the MgII index wavelet spectrum. The wavelet power spectrum within white areas is not shown due to corruption of the convolution procedure near the edges of some

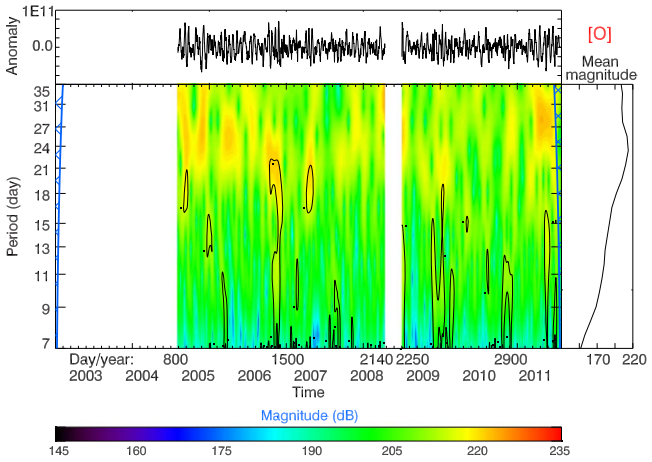

Fig. 5. The [O] anomaly time series is shown in the upper panel. The [O] wavelet power spectrum is shown in the main part of the figure and the temporally averaged spectrum is shown in the right part of the figure. The cone of influence region is marked in blue. The wavelet power spectrum within white areas is not shown due to corruption of the convolution procedure near the edges of some rare data gaps discussed in Section 3.2. The red contour line corresponds to the 99% confidence level and the black line to 68%. See Section 4.2.2 for further details. The horizontal axis includes the day numbering starting on January 1, 2003. (For interpretation of the references to color in this figure legend, the reader is referred to the web version of this article.)

rare data gaps discussed in Section 3.2. Particularly, the wavelet power spectrum in the time interval 2140 – 2250 days was chosen to be excluded due to the date gap with the duration of 18 days because the effective COI (not shown) around this date gap is about 100 days.

It is common for the [O], MgII index and Lyman-α wavelet spectra that they show the presence of the major 27-day periodicity in the time intervals corresponding to the solar maximum phase. The MgII index and Lyman-α wavelet spectra also exhibit the presence of the major 27-day periodicity during descending and ascending solar activity significant at the 68% confidence level.

4.2.3. Estimation of the phase shift of the atomic oxygen response to solar forcing using cross-correlation analysis

To determine the phase shift between the MgII index and the [O] anomaly data sets we applied the cross-correlation analysis technique. The [O] anomaly data sets were averaged in the altitude range 90 – 100 km for different time intervals as introduced in Section 3.2. The upper panel of Fig. 6 shows the results of this cross-correlation. The black solid and red dashed line correspond to the descending-phase and long time intervals, respectively. The time-lagged cross correlations for both time intervals evidently exhibit a strong signature with a period near 27 days.

As the upper panel of Fig. 6 shows, the cross-correlation values for both the descending-phase and long time series are significant at the 2-σ confidence level (see the gray dash-dotted and red dotted lines). The significance testing was performed using the random phase test described by Ebisuzaki (1997), i.e., a large number of random time series were generated from the anomaly time series having the same power spectra, but different phase. The significance of a given correlation coefficient was determined by comparing the correlation coefficient to the distribution of correlation coefficients of the random phase ensemble.

The black solid line shows a coherent oscillation with the temporal distance between the center minimum and the following minimum being about 27 days. The cross-correlation attains a maximum at a time lag of 13 days, which corresponds to our preliminary estimate of the phase shift between solar forcing and the [O] response. Comparing the time lags of the descending-phase and long time series (shown by the black solid and red dashed lines in the upper panel of Fig. 6) we find a

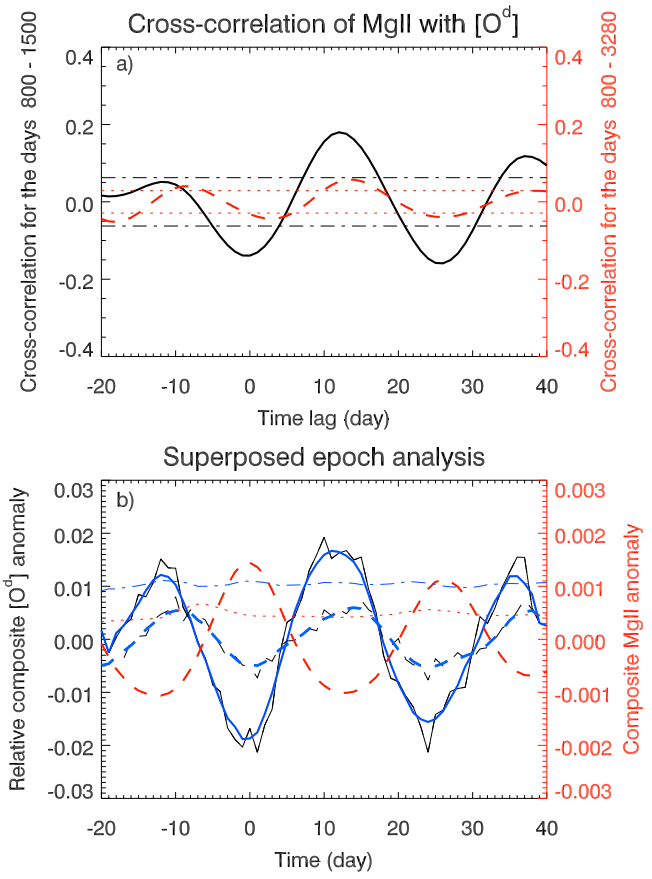

Fig. 6. Upper panel: Time-lagged cross-correlation between the MgII index and the daily [O] anomaly ([O^d]) data sets (black solid and red dashed lines correspond to the descending-phase and long time intervals introduced in Section 3.2). The gray dash-dotted and red dotted lines correspond to the 95% confidence levels for the descending-phase and long time intervals, respectively. Lower panel: The composite or superposed MgII index anomaly for the long time data set (red dashed curve) and the composite [O] anomaly for both the descending-phase data sets (solid blue line) and long data sets (blue dashed line). The blue dash-dotted (red dotted) line represents the 95% confidence level for the descending-phase (long) composite [O] anomaly data sets. The daily equatorial [O] anomaly data sets were averaged in the altitude range 90–100 km for time intervals as introduced in Section 3.2. See Sections 4.2.3 and 4.2.4 for further details. (For interpretation of the references to color in this figure legend, the reader is referred to the web version of this article.)

difference of about 2 days. These time delays could be caused by both physical and chemical drivers involved in the MLT region and are discussed in Section 4.6.

4.2.4. Estimation of the phase shift of the atomic oxygen response to solar forcing using the superposed epoch analysis (SEA) technique

Upon calculating the phase shift between the MgII index and the [O] anomaly data sets using the cross-correlation analysis, we applied another technique, i.e., the superposed epoch analysis (SEA) (Chree, 1913), which is also known as the composite technique. 61-day epochs were chosen in such a way that they are centered at maxima of the MgII index anomaly. The individual MgII and [O] epoch time series were then superposed as described in more detail in, e.g., Robert et al. (2010) or Thomas et al. (2015).

The lower panel of Fig. 6 shows the composite MgII anomaly (MgII^c, red dashed line) for the long data set and the composite [O] anomaly ([O^c]) for both the descending-phase (blue solid line) and long data sets (blue dashed line). The composite MgII anomaly shows the maximum at time lag zero, as expected. The composite MgII anomaly exhibits clear peaks about 25 – 27 days apart, corresponding to the 27-day signature of solar forcing. The thick blue composite [O] anomalies

correspond to 5-day running means. The original composite anomalies are also shown as thin lines. Note that the displayed composite [O] anomalies are relative anomalies, i.e., absolute anomalies divided by the average O concentration.

The blue dash-dotted curve shown in the lower panel of Fig. 6 represents the 95% confidence level for the descending-phase data set [O^c]. The confidence level was determined through application of the bootstrapping method (Blarquez and Carcaillet, 2010) that was performed in two steps. In the first step a randomization is performed, adding white noise to the signal. The Gaussian noise is characterized by a mean value equal to zero and a standard deviation corresponding to the average of daily standard errors of the mean of the oxygen anomaly. In the next step (known as random subset selection), the composite matrices from a large number of Monte Carlo simulations are randomly permuted. The red dotted curve shown in the lower panel of Fig. 6 represents the 95% confidence level for the [O^c] long data set.

The temporal distance between two clear [O^c] minima indicates the presence of a 25-day periodicity for the long time interval, and a 26-day periodicity for the descending-phase time interval that is shorter than the periodicity of about 27 days found from the cross-correlation analysis. Note that the results agree with each other within their uncertainties. The time lag from the center of the 61-day lag-window to the maximal peak of [O^c] (see solid blue thick line) is about 12 days, which is in very good agreement with the time lag obtained by the cross-correlation analysis.

If we compare the time lag between the [O] maximum and the MgII index for the descending-phase and long time series in the lower panel of Fig. 6, we again find a difference of about 2 days. The [O] anomaly maximum for the descending-phase time series occurs at about day 12, and the one for the long time series at about day 14. Being consistent with the cross-correlation analysis (upper panel of Fig. 6) the superposed epoch analysis leads to a slightly larger time lag for the long time series as compared to the descending-phase time series.

In summary, we find statistically significant 27-day signatures in MLT atomic oxygen with time lag of about 13 days relative to solar forcing and relative amplitudes on the order of 1%. In addition, the results obtained by applying the superposed epoch analysis technique are consistent with the cross-correlation analysis, which constitutes an important consistency check.

4.3. Quantitative estimation of atomic oxygen sensitivity to solar forcing based on annually and daily averaged [O] time series

The quantitative estimation of the [O] sensitivity to the 11-year and the 27-day solar cycles was performed with a regression analysis applied to relative [O] values and a solar proxy (MgII index or Lyman-α). Relative [O] values were calculated according to the following equation:

$$[O_r] = \frac{[O] - \langle [O] \rangle}{\langle [O] \rangle}, \tag{2}$$

where $\langle [O] \rangle$ denotes the averaged [O] time series. The annually averaged [O] time series (denoted with the upper index a as [O^a], see Section 4.1) were used to calculate the annually averaged relative values [O^a_r]. In terms of the 27-day sensitivity we already determined superposed or composite anomalies, which essentially correspond to the numerator of the Eq. (2). The sensitivity of atomic oxygen to solar forcing at the 27-day scale was determined by plotting the relative superposed [O^c] anomaly and the solar proxy anomaly in a scatter plot (see Fig. 7) and performing a linear regression. Additionally, the epoch averaged [O^c] data set was shifted with respect to the superposed epoch averaged MgII index or Lyman-α data set, so that the maximal value of [O^c] coincides with the maximal value of the solar proxy. The sensitivity is then simply given by the slope of the regression line.

The uncertainty of the calculated sensitivity was determined considering errors in both the atomic oxygen concentration and the solar proxy value (see Press et al. (1997) for more information on the χ^2 merit function to be minimized). The least-squares fitting was performed with the Levenberg-Marquardt algorithm implemented in the IDL routine MPFIT (Markwardt, 2009) and the uncertainty of the sensitivity was calculated with the reduced χ^2 function set to unity, following the MPFIT user's guide. This is justified here, because the fits were of good quality.

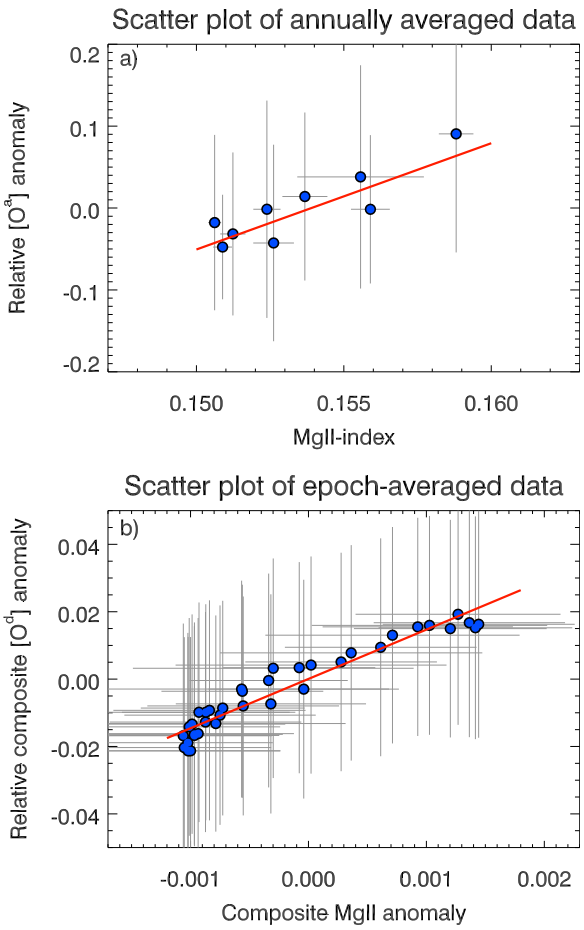

Fig. 7. Upper panel: Scatter plot of the annually averaged MgII index and relative [O] anomaly ([O^a])values. The slope of the regression line corresponds to the sensitivity. Lower panel: Scatter plot of the daily averaged values of the composite MgII index anomaly and the relative composite [O] anomaly ([O^d]) data sets. The slope of the regression line corresponds to the sensitivity. The equatorial [O] anomaly data sets were averaged in the altitude range 90–100 km for time intervals as introduced in Section 3.2. See Section 4.3 for further details. (For interpretation of the references to color in this figure legend, the reader is referred to the web version of this article.)

The upper panel of Fig. 7 shows a scatter plot of the annually averaged values of the MgII index and the relative [O] anomaly data sets. The [O] anomaly data sets were averaged in the altitude range 90–100 km. The sensitivity of atomic oxygen with respect to solar forcing represented by the MgII index corresponds to the slope of the linear regression. The sensitivity of [O^a] with respect to the MgII index data for the years 2003–2011 is β^a_{MgII}=13.0%(±3.0%)/(0.01 MgII index unit). To convert this sensitivity to the sensitivity with respect to the F10.7 cm radio flux we used the linear relationship between the F10.7 cm radio flux and the MgII index data, see Fig. 2 and Section 4.2. The F10.7 cm sensitivity corresponding to β^a_{MgII} is $\beta^a_{F10.7}$(MgII) = 17.2%(±3.9%)/(100 sfu).

We repeated the analysis using Lyman-α as the proxy indicator of solar activity, see Section 3.1 for further details. The values of sensitivity of [O] to the 11-year solar cycle calculated according to

Table 1
The values of sensitivity of atomic oxygen ([O]) to solar forcing were calculated using the time series of MgII index and Lyman-α as proxy indicators of solar activity and converted with respect to F10.7 cm radio flux measured in sfu. Different approaches applied enable us to compare the results for the 11-year and 27-day temporal scales. The values of daily averaged [O] time series were retrieved according to the well-known cubic equation and averaged over the 90–100 km altitude range. On the base of the annually averaged [O] time series ([O^a]) we calculated sensitivities of [O^a] to solar forcing (with help of the linear regression analysis) for the 11-year temporal scale. On the base of the monthly averaged [O] time series ([O^m]) we calculated the relative percentage changes of [O^m] for solar maximum conditions relative to the solar minimum (with help of the scaled values of the components of multiple-linear regression analysis) for the 11-year temporal scale. The calculated sensitivities of [O^a] and relative percentage changes of [O^m] correspond to the 11-year cycle of solar activity. On the base of the daily averaged [O] time series ([O^d]) we calculated sensitivities of [O^d] to solar forcing (with help of the superposed epoch analysis (SEA) and the linear regression analysis) for the 27-day temporal scale for conditions of the descending phase and the solar minimum of solar activity. See Sections 4.3 and 4.4 for further details.

Time ranges / Sensitivity	%/(0.01 MgII)	%/(1 LyA)	%/(100 sfu), use MgII	%/(100 sfu), use LyA	%, solar max- min, use MgII	%, solar max- min, use LyA
Annual averaging, 11-y	13.0 ± 3.0	9.4 ± 2.1	17.2 ± 3.9	15.9 ± 3.6	16.3 ± 3.7	15.1 ± 3.3
Monthly averaging, 11-y			12.8 ± 3.8	18.4 ± 6.6	12.2 ± 3.6	17.4 ± 6.3
Descending phase, 27-d	14.6 ± 0.7	14.9 ± 1.3	19.4 ± 0.9	25.1 ± 2.1	18.4 ± 0.9	23.9 ± 2.0
The solar minimum, 27-d	0.4 ± 1.4	0.3 ± 1.2	0.5 ± 1.9	0.5 ± 2.0	0.5 ± 1.8	0.5 ± 1.9

the method described above are shown in Table 1. The F10.7 cm sensitivity derived from the Lyman-α analysis is $\beta^{a}_{F10.7}(\mathrm{LyA}) = 15.9\%(\pm 3.6\%)/(100\ \mathrm{sfu})$.

We applied the superposed epoch method on the daily averaged [O] ([O^d]) time series and calculated the linear regression, the slope of which is shown in the lower panel of the Fig. 7 that represents the sensitivity of [O] to solar forcing on the 27-day temporal scale. The sensitivity of [O^d] with respect to the MgII index data for the descending phase of solar activity is $\beta^{d}_{MgII} = 14.6\%\ (\pm 0.7\%)/(0.01\ \mathrm{MgII\ index\ unit})$. We converted this sensitivity to the sensitivity with respect to the F10.7 cm radio flux, see Section 4.2 and Fig. 2 for further details. The obtained F10.7 cm sensitivity is $\beta^{d}_{F10.7}(\mathrm{MgII}) = 19.4\%(\pm 0.9\%)/(100\ \mathrm{sfu})$. We repeated the analysis using Lyman-α as the proxy indicator of solar activity and obtained the F10.7 cm sensitivity $\beta^{d}_{F10.7}(\mathrm{LyA}) = 25.1\%(\pm 2.1\%)/(100\ \mathrm{sfu})$. The sensitivity of [$O^d$] to solar forcing for the solar minimum phase was determined with help of the superposed epoch method and shown in the lowest row of the Tables 1 and 2 according to the well-known and the extended cubic equations.

The consistency of our results with earlier experimental and modeling results will be discussed in detail in Section 4.5, and the multiple-linear regression results are presented in the following Section 4.4.

4.4. Multiple-linear regression analysis of monthly averaged [O] time series

In order to identify and quantify the relevant sources of variability – including, e.g., solar impact, seasonal variation, or a long-term trend – in the monthly averaged [O] time series we performed a multiple-linear regression analysis including some elementary trigonometric functions. The following model was used to approximate the monthly averaged [O] ([O^m]) time series:

$$\begin{aligned} FIT(t) = {} & Offset + LT^{Amp}\cdot t + MgII^{Amp}\cdot MgII(t + MgII^{Pha}) \\ & + QBO_1^{Amp}\cdot\cos\left(\frac{2\pi t}{QBO_1^{Per}} + QBO_1^{Pha}\right) + QBO_2^{Amp}\cdot \\ & \cos\left(\frac{2\pi t}{QBO_2^{Per}} + QBO_2^{Pha}\right) + AO^{Amp}\cdot\cos\left(\frac{2\pi t}{AO^{Per}} + AO^{Pha}\right) \\ & + SAO^{Amp}\cdot\cos\left(\frac{2\pi t}{SAO^{Per}} + SAO^{Pha}\right). \end{aligned} \quad (3)$$

The upper indices of the variables denote the type of variable, i.e., *Amp* for amplitude in atoms cm^{-3}, *Per* for period and *Pha* for phase in months. The terms of the multiple-linear fit equation contain the following parameters: *Offset* is the offset, LT is the linear trend term, $\mathrm{MgII}^{\mathrm{Amp}}$ is the amplitude of the solar term, and MgII is the MgII index time series. $\mathrm{MgII}^{\mathrm{Pha}}$ is the phase shift of the MgII time series with respect to the [O^m] time series. Also considered are two quasi-biennial oscillation (QBO) terms consisting of the amplitudes $\mathrm{QBO}^{\mathrm{Amp}}$, cosine functions with periods $\mathrm{QBO}^{\mathrm{Per}}$ and phase shifts $\mathrm{QBO}^{\mathrm{Pha}}$. Moreover, an annual component is considered with amplitude $\mathrm{AO}^{\mathrm{Amp}}$, period $\mathrm{AO}^{\mathrm{Per}}$ and phase $\mathrm{AO}^{\mathrm{Pha}}$. The semi-annual oscillation (SAO) term is defined in a similar way as the QBO and AO terms.

Fig. 8 shows the [O^m] time series (green dots) averaged over the 0° to 20 °N latitude range and the 90 – 100 km altitude range. The blue line shows the result of the multiple-linear fit. The individual fitting terms represent the contributions of the corresponding processes or proxy variables to the fitted time series and are shown as blue solid lines in the lower panels of Fig. 8. The black dots in these panels correspond to the difference between the original [O^m] time series and the sum of all fitted components except the one under consideration.

The multiple-linear regression analysis was performed on the atomic oxygen retrieval based on the well-known cubic equation solution, as well as on the extended cubic solution. The multiple-linear fit results for the well-known cubic solution are shown in Fig. 8 and also presented in Table 3. Table 4 presents fit results for the extended cubic solution.

The multiple-linear regression analysis was performed with the Levenberg-Marquardt algorithm implemented in the IDL routine MPFIT (Markwardt, 2009). The procedure we used to carry out the

Table 2
Similar to Table 1, but for atomic oxygen profile retrievals based on the extended cubic equation.

Time ranges	%/(0.01 MgII)	%/(1 LyA)	%/(100 sfu), use MgII	%/(100 sfu), use LyA	%, solar max- min, use MgII	%, solar max- min, use LyA
Annual averaging, 11-y	5.6 ± 3.8	11.2 ± 2.7	20.6 ± 5.0	19.0 ± 4.6	19.6 ± 4.8	18.0 ± 4.4
Monthly averaging, 11-y			16.5 ± 4.2	22.1 ± 5.0	15.7 ± 4.0	21.0 ± 4.8
Descending phase, 27-d	15.6 ± 0.9	16.4 ± 1.5	20.7 ± 1.1	27.7 ± 2.6	19.7 ± 1.1	26.4 ± 2.5
The solar minimum, 27-d	1.2 ± 1.7	0.9 ± 1.3	1.6 ± 2.3	1.5 ± 2.2	1.6 ± 2.1	1.4 ± 2.1

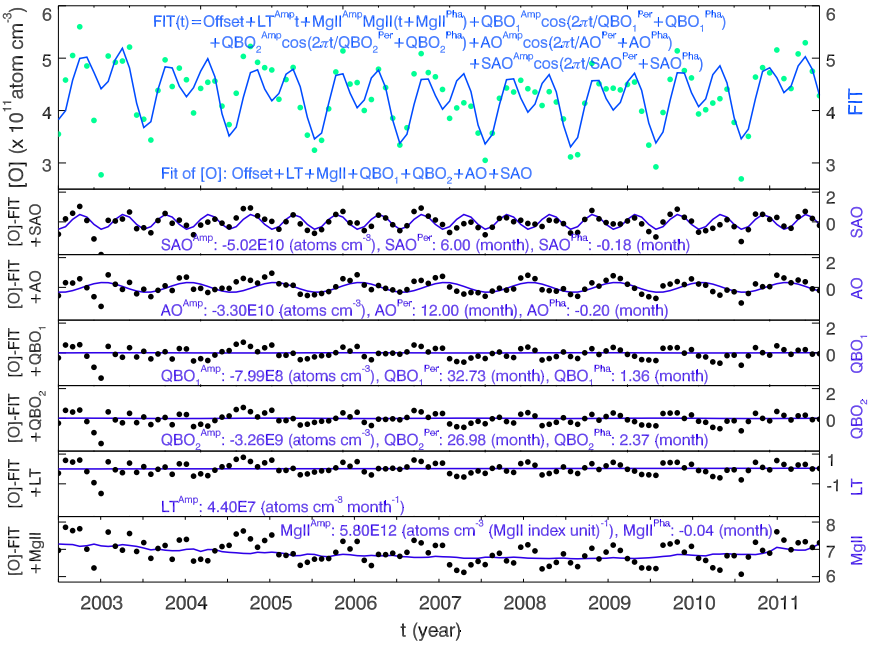

Fig. 8. Multiple-linear fit of the monthly averaged [O] ([O^m]) data set with consideration of the MgII index as a proxy of solar activity. The [O^m] time series was averaged in the latitude range 0° – 20 °N and the altitude range 90–100 km. The upper panel contains values of the [O^m] data set (green dots), the resulting fit curve (blue solid line) calculated with help of the fit equation (containing the terms and parameters shown above the fit curve). The parameters of the fit equation terms are discussed in Section 4.4. The time series of single components (the superposition of which gives the fitted time series in the upper panel) are represented in lower panels (violet lines) calculated for the terms of the fitting equation. The black dots in the lower panels correspond to the difference between the original [O^m] time series and the sum of all fitted components except the one under consideration. (For interpretation of the references to color in this figure legend, the reader is referred to the web version of this article.)

multiple-linear fit consisted of a sequence of five steps to determine optimal values of the fitting parameters with the minimal degree of freedom. The procedure is based on setting the input parameter values at a given fitting step to the values determined by the previous steps. At each step the optimal values of the fitting parameters were chosen from the range of possible values at the minimum of the χ^2 function. The values of the reduced χ^2 function were chosen to be equal to one to calculate the uncertainty of the fitting parameters.

In the first step of the procedure we fixed the values of several parameters, i.e.:

(a) the phase shift of the MgII index time series $MgII^{Pha}$ was set to 13 days according to the SEA and cross-correlation analyses, see Section 4.2.3 and Section 4.2.4,
(b) the period of semi-annual oscillation (SAO^{Per}) was set to 6 months,
(c) the period of annual oscillations (AO^{Per}) was set to 12 months,

and set initial values for the parameters QBO_1^{Amp}, QBO_1^{Per}, QBO_1^{Pha}, QBO_2^{Amp}, QBO_2^{Per}, QBO_2^{Pha}, SAO^{Amp}, SAO^{Pha}, AO^{Amp} and AO^{Pha} according to the discussion by Baldwin et al. (2001) and Burrage et al. (1996). The initial values for the parameters LT^{Amp} and $MgII^{Amp}$ were obtained during a test fit of the [O^m] time series with other parameters being constrained as it is described above.

We then applied a band pass filter to the [O^m] time series in order to find optimal values of the phases of the annual (AO^{Pha}) and semi-annual (SAO^{Pha}) oscillations in the following way. The technique of bandpass filtering by consecutive smoothing (see Section 4.2 for further details) was applied to the initial [O^m] time series to determine AO^{Pha}. For instance, we analyzed the anomaly time series obtained through removal of a 19-month running mean followed by smoothing with a 9-month running mean. The resulting filtered time series was then fitted by a three-parameter sinusoidal function to yield AO^{Pha}. SAO^{Pha} was determined in a similar way: we analyzed the anomaly time series obtained through removal of a 9-month running mean followed

Table 3
The sensitivity values of atomic oxygen ([O]) to solar forcing were calculated using the time series of MgII index and Lyman-α as proxy indicators of solar activity and converted with respect to F10.7 cm radio flux measured in sfu. The values of daily averaged [O] time series were retrieved for the years 2003 – 2011 according to the well-known cubic equation. The [O] time series were averaged annually and monthly and additionally averaged in the altitude ranges shown in the table header. On the base of the annually averaged [O] time series ([O^a]) we calculated sensitivities of [O^a] to solar forcing (with help of the linear regression analysis) for the 11-year temporal scale. On the base of the monthly averaged [O] time series ([O^m]) we calculated the relative percentage changes of [O^m] for solar maximum conditions relative to the solar minimum (with help of the scaled values of the components of multiple-linear regression analysis) for the 11-year temporal scale. The calculated sensitivities of [O^a] and relative percentage changes of [O^m] correspond to the 11-year cycle of solar activity. See Sections 4.3 and 4.4 for further details.

Time ranges / Altitude range (km)	88 – 90	91 – 93	94 – 96	97 – 99	100 – 102	90 – 100
Annual averaging, $\beta^a_{F10.7}$(MgII) (%/100 sfu), use MgII	8.7 ± 5.6	8.2 ± 6.6	19.5 ± 4.3	26.2 ± 5.8	26.6 ± 13.0	17.2 ± 3.9
Annual averaging, $\beta^a_{F10.7}$(LyA) (%/100 sfu), use LyA	7.5 ± 5.6	6.8 ± 6.2	17.7 ± 4.2	24.5 ± 4.5	26.3 ± 11.1	15.9 ± 3.6
Annual averaging, $\beta^a_{\%-11y}$(MgII) (%), solar max - min, MgII	8.2 ± 5.3	7.8 ± 6.2	18.5 ± 4.0	24.8 ± 5.5	25.2 ± 12.3	16.3 ± 3.7
Annual averaging, $\beta^a_{\%-11y}$(LyA) (%), solar max - min, LyA	7.1 ± 5.3	6.5 ± 5.9	16.8 ± 4.0	23.3 ± 4.2	25.0 ± 10.5	15.1 ± 3.3
Monthly averaging, $\beta^m_{\%}$(MgII) (%), use MgII	5.3 ± 7.2	10.5 ± 4.3	12.9 ± 4.2	15.7 ± 3.8	20.0 ± 5.4	12.8 ± 3.8
Monthly averaging, $\beta^m_{\%}$(LyA) (%), use LyA	7.2 ± 7.1	12.8 ± 5.4	16.7 ± 5.2	19.8 ± 6.8	24.2 ± 6.2	18.4 ± 6.6
Monthly averaging, $\beta^m_{\%-11y}$(MgII) (%), solar max - min, MgII	5.0 ± 6.9	10.0 ± 4.1	12.3 ± 4.0	14.9 ± 3.6	19.0 ± 5.1	12.2 ± 3.6
Monthly averaging, $\beta^m_{\%-11y}$(LyA) (%), solar max - min, LyA	6.9 ± 6.8	12.1 ± 5.1	15.9 ± 4.9	18.8 ± 6.5	23.0 ± 5.9	17.4 ± 6.3

Table 4
Similar to Table 3, but for atomic oxygen profile retrievals based on the extended cubic equation.

Time ranges / Altitude range (km)	88 – 90	91 – 93	94 – 96	97 – 99	100 – 102	90 – 100
Annual averaging, $\beta^{a}_{F10.7}$(MgII) (%/100 sfu), use MgII	10.6 ± 6.9	10.9 ± 7.9	22.2 ± 5.5	32.4 ± 6.5	31.5 ± 11.9	20.6 ± 5.0
Annual averaging, $\beta^{a}_{F10.7}$(LyA) (%/100 sfu), use LyA	9.0 ± 6.8	9.2 ± 7.5	20.2 ± 5.3	30.2 ± 5.0	30.5 ± 10.0	19.0 ± 4.6
Annual averaging, $\beta^{a}_{\%-11y}$(MgII) (%), solar max - min, MgII	10.0 ± 6.5	10.3 ± 7.5	21.1 ± 5.2	30.9 ± 6.2	29.9 ± 11.3	19.6 ± 4.8
Annual averaging, $\beta^{a}_{\%-11y}$(LyA) (%), solar max - min, LyA	8.5 ± 6.4	8.7 ± 7.1	19.2 ± 5.1	28.6 ± 4.7	29.0 ± 9.5	18.0 ± 4.4
Monthly averaging, $\beta^{m}_{\%}$(MgII) (%), use MgII	7.8 ± 5.0	12.7 ± 5.2	16.4 ± 4.8	19.5 ± 4.5	23.7 ± 13.3	16.5 ± 4.2
Monthly averaging, $\beta^{m}_{\%}$(LyA) (%), use LyA	9.5 ± 6.1	16.0 ± 6.4	20.3 ± 5.9	24.3 ± 5.0	28.4 ± 26.4	22.1 ± 5.0
Monthly averaging, $\beta^{m}_{\%-11y}$(MgII) (%), solar max - min, MgII	7.4 ± 4.8	12.0 ± 5.0	15.5 ± 4.6	18.5 ± 4.3	22.6 ± 12.6	15.7 ± 4.0
Monthly averaging, $\beta^{m}_{\%-11y}$(LyA) (%), solar max - min, LyA	9.1 ± 5.8	15.2 ± 6.1	19.3 ± 5.6	23.1 ± 4.7	27.0 ± 25.0	21.0 ± 4.8

by smoothing with a 3-month running mean.

In the second step we fixed the values of the variables studied in the first step to calculate χ^2 (Markwardt, 2009). We then varied the amplitudes of the semi-annual and annual oscillations (SAO^{Amp}, AO^{Amp}) to determine their optimal values corresponding to the minimum of the χ^2 function.

In the third step we fixed the values of all variables dealt with in the previous steps and calculated χ^2. We then applied the technique of bandpass filtering by consecutive smoothing (see Section 4.2 for further details) to the initial [O^m] time series two times to determine optimal values for the periods and phases of the QBO components (i.e., QBO_1^{Per}, QBO_1^{Pha}, QBO_2^{Per}, QBO_2^{Pha}). For instance, to determine optimal values for QBO_1^{Per} and QBO_1^{Pha} we analyzed the anomaly time series obtained through removal of a 29-month running mean followed by smoothing with a 12-month running mean. And to determine optimal values for QBO_2^{Per} and QBO_2^{Pha} we analyzed the anomaly time series obtained through removal of a 50-month running mean followed by smoothing with a 29-month running mean.

In the following fourth step we fixed again the values of all parameters studied so far and calculated χ^2. Then we varied the values of the amplitudes of the QBO components (i.e, QBO_1^{Amp}, QBO_2^{Amp}) to determine their optimal values corresponding to a χ^2 minimum.

In the fifth step we fixed the values of all parameters studied in the previous steps and calculated χ^2. Then we determined the optimal values of the amplitude of the shifted MgII index time series and the linear terms (i.e., LT^{Amp}, $MgII^{Amp}$) as described in the previous steps.

The described fitting procedure was then repeated once including the determined optimal values of the fitting parameters to improve the fit quality.

We now discuss the results obtained by performing the described multiple-linear analysis and compare them to results based on the regression analysis presented in Section 4.3. The upper panel of Fig. 9 shows the sensitivity of atomic oxygen to the solar forcing at the 11-year time scale estimated for annually averaged data sets as a function of altitude using the regression analysis as described in Section 4.3. The red and blue dots in this panel correspond to the O sensitivity values with respect to the F10.7-cm radio flux (see Section 4.3) calculated from the sensitivity with respect to Lyman-α (blue dots) and MgII index (red dots).

The most obvious feature of the upper panel of Fig. 9 is the increase in sensitivity with increasing altitude, with values of about 10% near 90 km and about 20–30% near 100 km. This result is as expected and is consistent with the analysis recently presented by Zhu et al. (2015). We also note that the [O] sensitivity values based on the MgII index and Lyman-α are very consistent and agree well within uncertainties.

In several earlier studies (Schmidt et al., 2006; Marsh et al., 2007) the O response to the 11-year solar variation is presented as the relative difference in O abundance between the solar maximum and minimum. In order to allow for an easy comparison with these results, we determined the same quantity based on the sensitivity values derived in our study in the following way: the sensitivity values were multiplied

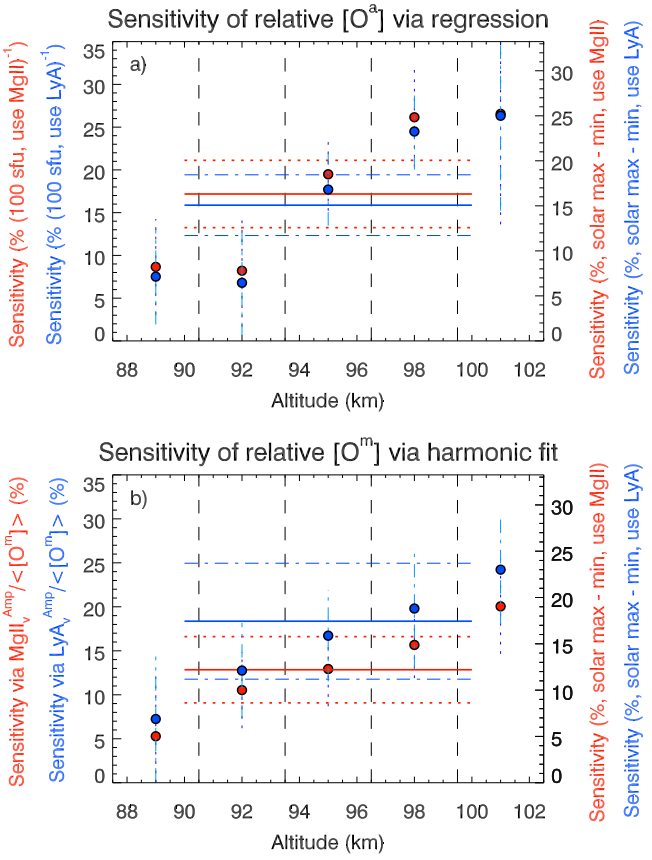

Fig. 9. Upper panel: sensitivity values estimated according to the regression analysis of the annually averaged entire data sets. Lower panel: sensitivity values estimated according to the multiple-linear regression analysis (harmonic fit) of the monthly averaged entire data sets. Right ordinates in the upper and lower panels show relative percentage changes of atomic oxygen for solar maximum conditions relative to the solar minimum. Left ordinates in the panels show the originally calculated sensitivities that were used to estimate the relative percentage changes at the right ordinates, see the first and the last line in the Table 1. See Sections 3.2 and 4.4 for further details. (For interpretation of the references to color in this figure legend, the reader is referred to the web version of this article.)

by the difference between the maximum and minimum F10.7 cm flux values to yield relative differences in atomic oxygen concentration between the solar maximum and minimum. These relative atomic oxygen differences are also shown in the upper panel of Fig. 9 (see right ordinate).

The red horizontal line represents the sensitivity with respect to the F10.7 cm flux determined using the MgII index – the blue line similarly shows the sensitivity based on the Lyman-α analysis – if the [O^a] time series is averaged over the 90 – 100 km altitude range. The dashed red horizontal lines represent the 68% confidence level of the sensitivity

based on the MgII index. The dash-dotted blue horizontal lines represent the 68% confidence level of the sensitivity based on Lyman-α.

The lower panel of Fig. 9 shows the ratio of the fitted amplitude of MgII index component ($MgII_v^{Amp}$) and Lyman-α (LyA_v^{Amp}) to $\langle[O^m]\rangle$, i.e., to the monthly averaged $[O^m]$ for the years 2003 – 2011 and averaged over 5 altitude ranges (88 – 90 km, 91 – 93 km, 94 – 96 km, 97 – 99 km and 100 – 102 km).

The right ordinate of the lower panel of Fig. 9 shows the relative differences in atomic oxygen between the solar maximum and minimum obtained by the multiple-linear regression and based on both the MgII index and Lyman-α.

The red horizontal line represents the sensitivity with respect to the $MgII_v^{Amp}$ and the blue horizontal line – the sensitivity with respect to the LyA_v^{Amp}, where the $[O^a]$ time series was averaged in the 90 – 100 km altitude range. The dashed red horizontal lines represent the 68% confidence level of the sensitivity with respect to $MgII_v^{Amp}$. The dash-dotted blue horizontal lines represent the 68% confidence level of the sensitivity with respect to LyA_v^{Amp}.

The sensitivity values obtained through the multiple-linear regression analysis (see the lower panel of Fig. 9 and Table 3) are approximately equal to the sensitivity values obtained by the initial regression analysis (see the upper panel of Fig. 9 and Table 1 discussed in Section 4.3) at the 11-year time scale. However, the uncertainties of the sensitivity values based on the multiple-linear regression analysis are higher than those ones obtained from the latter method.

In terms of the other fit components of the multiple-linear regression analysis, we find.

(a) the linear trends to be very small and not statistically significant. For the 90–100 km altitude range the relative trends are 0.09 (± 0.30) %/year using the MgII index as a solar proxy. If Lyman-α is used the relative trends correspond to 0.36 (± 0.34) %/year.
(b) semi-annual and annual components with amplitudes on the order of 12% and 7% (i.e., peak to peak changes of about 25% and 15%), respectively.
(c) QBO signatures to be very small and statistically insignificant.

The decrease in values of several proxies of solar activity (MgII index, Lyman-α flux and solar F10.7 cm flux) estimated over the 22nd, 23rd and 24th solar cycles (not shown) implies a decline in solar forcing in the recent decades. This long-term trend is valid during the SCIAMACHY operation time as well. However, it is remarkable that the linear trend in [O] values estimated with help of the multiple-linear regression for the years 2003 – 2011 is positive, and not significant. The strong semi-annual oscillations found in the current study are consistent with the tidal influence, for which the semi-annual variation in meridional wind amplitude was described by McLandress et al. (1996).

We note that the sensitivities of [O] to solar forcing based on O retrievals with the extended cubic equation (see Table 2) are slightly larger than for the well-known cubic equation (see Table 1), but the values agree within their uncertainties. Tables 5, 6 present all the multiple-linear fit results as a function of altitude and for both the well-known cubic (Table 5) and the extended cubic equation (Table 6). The multiple-linear fit results for the well-known cubic and the extended cubic solution differ somewhat, but are in good overall agreement (cf. Tables 5 and 6).

4.5. Comparison to earlier results

We now compare the main results of the current study with published experimental and modeling results and start with 11-year solar cycle variations in MLT atomic oxygen. Schmidt et al. (2006) presented model simulations with the HAMMONIA model showing a relative variation in atomic oxygen in the 90 – 100 km altitude range of about 15 – 20% between the solar maximum and minimum at the low latitudes studied here (their Fig. 12). Marsh et al. (2007) presented WACCM results corresponding to a relative variation in MLT atomic oxygen between 20% and 30% for these altitude and latitude ranges. Our relative variations in MLT atomic oxygen between the solar maximum and minimum are shown in Fig. 9 and correspond to values between 10% and 25%, increasing with altitude. Thus, we find reasonable overall agreement between our results and the model results presented by Schmidt et al. (2006) and Marsh et al., 2007. The altitude dependence seen in the SCIAMACHY data cannot be clearly identified in these studies. This altitude dependence, however, is present in an independent MLT atomic oxygen data set also retrieved from SCIAMACHY nightglow observations of the oxygen green line (Zhu et al., 2015).

In terms of solar 27-day signatures in MLT atomic oxygen we are not aware of any previous experimental studies, but a comparison of our results is possible with the HAMMONIA simulations analyzed by Gruzdev et al. (2009). Gruzdev et al. (2009) reported on sensitivities and time lags of atomic oxygen (amongst other species) to solar forcing at the 27-d scale. According to Fig. 10 in Gruzdev et al. (2009), the modeled sensitivity of atomic oxygen at low latitudes and altitudes between 90 and 100 km falls between 0.3% and 1% /(% change in 205 nm irradiance). During solar maximum conditions, the solar 27-day cycle in solar irradiance at 205 nm has an amplitude of about 2% (see Fig. 1 in Gruzdev et al. (2009)). This implies that for solar maximum conditions the HAMMONIA simulations produce an atomic oxygen variation with an amplitude of about 0.6 – 2%. The amplitudes determined in the present study are about 1.5% for the descending-phase data set (descending phase of solar cycle 23) and about 0.5% for the entire data set (our Fig. 6). In other words, we find good agreement in terms of the amplitude of the solar 27-day signature in MLT atomic oxygen with the HAMMONIA simulations presented by Gruzdev et al.

Table 5
Results of the multiple-linear regression based on the [O] profile retrievals according to the well-known cubic equation. The initial [O] time series with monthly resolution ($[O^m]$) for the years 2003 – 2011 was additionally averaged in the altitude ranges shown in the table header. The results are shown separately for fits performed with both the MgII index and the Lyman-α flux as solar proxies. The values of the periodic components correspond to the peak-to-peak values, i.e. two times the corresponding amplitude. See Section 4.4 for further details.

Component / Altitude range (km)	88 – 90	91 – 93	94 – 96	97 – 99	100 – 102	90 – 100
Linear trend (%/year), use MgII	0.24 ± 0.31	0.29 ± 0.34	0.07 ± 0.34	0.17 ± 0.31	0.06 ± 0.45	0.09 ± 0.30
Linear trend (%/year), use LyA	0.36 ± 0.54	0.46 ± 0.46	0.31 ± 0.38	0.16 ± 0.51	0.17 ± 0.44	0.36 ± 0.34
Annual oscillation (%), MgII	17.52 ± 0.50	22.19 ± 0.54	19.48 ± 0.51	10.40 ± 0.42	7.38 ± 0.47	15.33 ± 0.43
Annual oscillation (%), LyA	17.15 ± 3.14	22.49 ± 10.14	19.75 ± 18.71	12.82 ± 3.89	6.01 ± 2.91	15.61 ± 2.35
Semi-annual osc. (%), use MgII	26.97 ± 0.76	26.20 ± 0.65	22.60 ± 0.59	22.02 ± 0.89	23.90 ± 1.51	23.33 ± 0.66
Semi-annual osc. (%), use LyA	26.60 ± 4.86	26.10 ± 11.75	22.51 ± 21.34	21.28 ± 6.48	24.16 ± 11.71	23.42 ± 3.52
Long-periodical QBO (%), MgII	1.70 ± 2.98	1.54 ± 3.87	0.06 ± 3.26	0.17 ± 2.66	2.52 ± 3.54	0.37 ± 3.03
Long-periodical QBO (%), LyA	1.85 ± 2.99	1.26 ± 4.10	0.01 ± 3.26	0.44 ± 2.90	1.39 ± 2.81	2.60 ± 12.55
Short-periodical QBO (%), MgII	1.95 ± 3.42	0.19 ± 0.48	0.06 ± 15.01	1.13 ± 17.27	3.22 ± 4.51	1.52 ± 4.69
Short-periodical QBO (%), LyA	1.75 ± 2.82	0.31 ± 1.00	0.01 ± 3.26	1.61 ± 10.66	3.01 ± 6.14	1.03 ± 4.97

Table 6
Similar to Table 5, but for atomic oxygen profile retrievals based on the extended cubic equation.

Component / Altitude range (km)	88 – 90	91 – 93	94 – 96	97 – 99	100 – 102	90 – 100
Linear trend (%/year), use MgII	0.32 ± 0.39	0.32 ± 0.40	0.09 ± 0.39	0.12 ± 0.37	0.04 ± 1.11	0.06 ± 0.34
Linear trend (%/year), use LyA	0.44 ± 0.44	0.55 ± 0.46	0.40 ± 0.43	0.23 ± 0.37	0.34 ± 0.05	0.41 ± 0.36
Annual oscillation (%), MgII	21.59 ± 4.99	26.22 ± 4.16	21.98 ± 19.83	10.60 ± 5.70	40.31 ± 5.15	17.63 ± 3.89
Annual oscillation (%), LyA	20.90 ± 0.60	26.79 ± 2.15	22.50 ± 0.58	10.41 ± 1.05	11.27 ± 0.47	17.79 ± 0.49
Semi-annual osc. (%), use MgII	32.43 ± 7.46	31.48 ± 4.99	26.82 ± 24.18	25.41 ± 14.39	25.76 ± 3.30	27.49 ± 6.07
Semi-annual osc. (%), use LyA	32.17 ± 0.92	31.08 ± 2.49	26.97 ± 0.70	24.97 ± 2.52	25.92 ± 1.09	27.43 ± 0.75
Long-periodical QBO (%), MgII	1.64 ± 3.52	3.19 ± 4.82	0.41 ± 3.77	1.47 ± 3.53	0.09 ± 10.16	4.11 ± 3.37
Long-periodical QBO (%), LyA	1.73 ± 3.49	3.19 ± 4.85	0.60 ± 3.68	0.78 ± 3.13	1.16 ± 19.50	6.30 ± 13.49
Short-periodical QBO (%), MgII	3.15 ± 6.76	0.10 ± 0.14	3.00 ± 27.49	2.35 ± 5.64	0.13 ± 15.24	0.21 ± 0.17
Short-periodical QBO (%), LyA	2.91 ± 5.85	0.05 ± 0.07	3.19 ± 19.83	1.87 ± 7.47	2.54 ± 42.93	1.82 ± 3.92

(2009).

We now briefly discuss the model and experimental results on the time lag between solar forcing and the response in atomic oxygen at the 27-day scale. As shown in Fig. 6, the time lag between solar forcing and the response in atomic oxygen in our study is 12 – 14 days, depending on whether the descending-phase or long time series is considered. Gruzdev et al. (2009) report on a time lag of about a quarter 27-day cycle, i.e., about 4.5 – 7 days in the MLT. Thus, the time lag found in our study is about a quarter cycle longer than the model result by Gruzdev et al. (2009).

Regarding the time lag between 27-day solar forcing and the atmospheric response it is also interesting to compare SCIAMACHY OH(3-1) rotational temperature observations (analyzed by von Savigny et al. (2012) for the latitude range 0° – 20 °N) with the HAMMONIA temperature results discussed by Gruzdev et al. (2009). SCIAMACHY limb emission spectra at about 85 km tangent height were used to retrieve OH* volume emission rate profiles (von Savigny et al., 2012). The calculated SCIAMACHY rotational temperatures present averages over a certain altitude range, weighted by the vertical variation of the OH* volume emission rate (von Savigny et al., 2004). The effective emission altitude is about 87 km for the OH* temperature retrievals. The SCIAMACHY analysis of temperature shows a statistically highly significant 27-day signature that is in phase with solar forcing with the time lag of 1-day at most, while Gruzdev et al. (2009) report a time lag of about 4 – 6 days (i.e., 4.2 – 5.9 days in the altitude range 80 – 92 km and 2.5 – 4.2 days in the altitude range 92 – 100 km for the latitude range 0° – 20°N). This might imply that radiative damping considered in the HAMMONIA simulations is relatively slow, but not negligible. Gruzdev et al. (2009) mentioned that atomic oxygen is generated mainly by the photolysis of molecular oxygen in the mesosphere and found the response of HAMMONIA [O] above 85 km to be roughly in opposite phase with the response of molecular oxygen.

4.6. Discussion of possible mechanisms

Solar 27-day signatures have been identified in several experimental MLT data sets, including NLCs (Robert et al., 2010; von Savigny et al., 2013), ozone (Hood, 1986), temperature (Hood, 1986; von Savigny et al., 2012; Thomas et al., 2015), water (Thomas et al., 2015), OH * emission rate and emission altitude (Teiser and von Savigny, 2016). However, the underlying physico-chemical mechanisms driving these atmospheric responses to the 27-day solar forcing deserve further studies. Increased solar irradiance will lead to increased diabatic heating if other chemical or dynamical responses are neglected. Any photochemical response – e.g., altered production of ozone – may affect diabatic heating and/or radiative cooling. Moreover, chemical changes may lead to altered chemical heating due to exothermic chemical reactions that play an important role in the MLT energy budget. In addition, the solar forcing may affect atmospheric dynamics and lead to changes in upwelling, i.e., adiabatic heating/cooling.

In terms of the solar 27-day signatures in NLCs, there is increasing evidence for a dynamical mechanism: (a) the sensitivity of temperature to solar forcing at the 27-day temporal scale reaches its maximum in the polar summer mesopause, where gravity-wave driven adiabatic cooling also reaches its maximum (see Fig. 20.6 in von Savigny et al., 2013); (b) 27-day signatures in polar summer mesopause temperature and H_2O are almost exactly out-of-phase, whereas the latter is 180° shifted with respect to solar forcing (Thomas et al., 2015). Due to the long lifetime of H_2O at mesopause altitude, this time lag is not consistent with pure photodissociation of H_2O.

Concerning the 27-day signature identified in atomic oxygen, we follow Thomas et al. (2015) and distinguish between two different interpretations. The first interpretation supposes that the observed 27-day signature in atomic oxygen is caused only by photochemistry and/or radiative effects. The photochemical processes are mainly associated with the production of atomic oxygen at higher altitudes. The second interpretation involves dynamical effects, particularly, changes in vertical winds that lead to redistribution of atomic oxygen. Additionally, turbulence (eddy diffusion) and the large-scale mesospheric meridional circulation play a key role – the latter mainly at high latitudes. The dynamical processes are also associated with the vertical advection of atomic oxygen by eddy diffusion and the above mentioned large-scale circulation. The $[O]/[O_2]$ ratio increases with altitude in the MLT region and is affected by the strength of eddy diffusion (Colegrove et al., 1965). Vertical advection associated with tides and the large-scale circulation plays a major role in the seasonal variations according to the study of Liu et al. (2008), which is based on zonally averaged WINDII data analyzed in the latitude range 40 °S – 40°N. Liu et al. (2008) concluded that the vertical advection associated with the tides plays a relatively more important role than eddy diffusion. Liu et al. (2008) observed the dominant influence of the diurnal tide (at the equator) and a clearly semidiurnal pattern (at midlatitudes). Particularly, the diurnal tide enhances the green line emission from the early evening till about 23:00 LT at the equator. Note that SCIAMACHY performed observations from a sun-synchronous orbit at 22:00 LT when the dynamical influence of the meridional component of the diurnal migrating tide reaches its maximum (Ward, 1999). The influence of the diurnal tide on the greenline nightglow emission is tremendous at the equator (e.g., Burrage et al., 1996; Angelats i Coll and Forbes, 1998; Ward, 1999).

As for the results on the 27-day signature in atomic oxygen:

First, as the starting point, we can accept that the photochemical interpretation based on HAMMONIA (Gruzdev et al., 2009) implies the [O] time lag of 4.5 – 7 days with respect to 27-day solar forcing, whereas the analysis of SCIAMACHY data gives a time lag of half of the 27-day cycle, about 13 days. Thus, in the case of [O] there is a difference of about a quarter of cycle between the time lag found by Gruzdev et al. (2009) and the time lag determined from SCIAMACHY, see Section 4.5. Note that the temperature response to solar forcing (Gruzdev et al., 2009) is characterized by the time lag of about 4 – 6 days, whereas SCIAMACHY analysis of temperature (von Savigny et al., 2012) shows the time lag of one day at most, see Section 4.5. The

reason for the differences in the time lags is currently not known.

Second, dynamical interpretation would imply that the 27-day signature in atomic oxygen is caused by 27-day modulations of vertical winds. In this case, one would expect the temperature and atomic oxygen signatures to be in-phase because, e.g., enhanced upwelling leads to increased adiabatic cooling and a reduction of atomic oxygen. Both mesopause rotational temperature discussed by von Savigny et al. (2012) and [O] observations discussed in this paper were taken on the night-side of the SCIAMACHY orbit. Upon the assumption that temperature and [O] observations were affected by the diurnal tide, one could expect them also to be in-phase. However, the 27-day signatures in mesopause temperature and atomic oxygen are almost exactly out-of-phase (cf. Fig. 6 in this article and Fig. 3 in von Savigny et al., 2012). We averaged [O] time series in different altitude ranges (i.e., 88 – 90 km, 91 – 93 km, 94 – 96 km, 97 – 99 km and 100 – 102 km) to analyze the time lag between [O] and MgII time series with help of the cross-correlation technique. Provided that the vertical wavelength of the diurnal tide is about 25 km, it is hard to argue in favor of tidal influence because of little changes in values of the time lag corresponding to the altitude ranges between 91 and 102 km. Nevertheless, the resulting figure presenting the averaged time lags (not shown) exhibits a negative value of the [O] time lag corresponding to the altitude range 88 – 90 km. Note that the time lag of the mesopause rotational temperatures at a bit lower altitude is about zero (von Savigny et al., 2012). Taking this into account could presumably credit in favor of dynamical interpretation, provided that certain processes, which are responsible for the presence of such observations, would be known. In terms of lunar effects on O(^{1}S – ^{1}D) and OH* airglow emissions, [O] and temperature, the recent study by von Savigny et al. (2015) demonstrates that the phase relationship of the lunar semidiurnal tidal signatures in these quantities is consistent with the following sequence of processes: enhanced upwelling leads to cooling, a reduction in [O] and, consequently, a reduction in airglow emissions. In the case of the lunar tides, a relationship between temperature and [O] found by von Savigny et al. (2015) is consistent with vertical advection and adiabatic cooling. However, the temperature and [O] 27-day signatures presented in this paper seem not to be in-phase, and a dynamical interpretation might fail. So far, we have to admit that our results on the 27-day signature in MLT atomic oxygen concerning the time lag of [O] response to solar forcing are not directly in favor of either photochemical or dynamical interpretation. A quantitative analysis of the linearized continuity equation of [O] by accounting for the fact that the dynamical contributions are aliased by the tide because of SCIAMACHY's sun-synchronous sampling should be performed in order to identify the right mechanism. Additionally, dedicated model simulations considering all relevant processes are required – which are far beyond the scope of the present study. The studies mentioned below are supposed to be helpful to work out the frames and context of such model simulations. Possible sources for the 27-day variations in vertical advection are discussed by Pancheva et al. (2003) who investigated semidiurnal tide modulations (at about 53.5 °N latitude) that were positively correlated with the 27-day solar activity. Additionally, Pancheva et al. (2003) reasoned that the modulations of the semidiurnal tide probably could be produced by local nonlinear interaction if the time lag were significantly longer than a few days. Note that the semidiurnal amplitude modulations and similar variations in total ozone were found (Pancheva et al., 2003) with periods of 25 – 28 days (and other ones). It is interesting to note that the GLS spectrum of the [O^d] anomaly (see Section 4.2.1) shows peaks with close periods. Eckermann et al. (1997) analyzed interseasonal (10 – 100 days) oscillations in the equatorial MLT based on five years of velocity data acquired by a radar system at Christmas Island (2 °N). They identified strong peaks in zonal winds at periods of about 22 – 25 days (and other ones) as well as strong variations in diurnal tidal amplitudes with periods of about 25 days (and other ones). Pancheva (2001) observed tidal modulations in radar data (measured at about 53.5 °N, 42.5 °N and 67.9 °N) exhibiting 25-27 day periodicities and other ones. Luo et al. (2001) suggested that a 25-29 day (23-32 day) oscillations could be produced by a nonlinear interaction between annual (semiannual) and 27-day variations. As we concluded in Section 4.2.1, the impact of oscillations should have been canceled out in cross-correlation and superposed epoch analyses if the time series were sufficiently long.

As for the sensitivity of [O] response to solar forcing:

The values of [O] sensitivity to solar forcing at the 27-day time scale during the descending phase of solar cycle 23 (see Tables 1 and 2, third line) and those ones at the 11-year time scale (see Tables 1 and 2, first and second lines, two last columns) are in good agreement. The similarity in [O] sensitivity indicates presence of similar driving processes in the MLT both at the 27-day and the 11-year time scales. Particularly, Solar Mesosphere Explorer and SBUV data sets show similarity of the approximate percentage values of the incoming solar irradiance variation in the far-ultraviolet region both at the 27-day and at the 11-year time scales (Rottman, 1988). Tables 1 and 2, last row, show that the [O] sensitivity at the 27-day time scale was significantly lower during the last solar minimum phase. A possible explanation of such a result could be based on the fact that the thermosphere was lower in density (and, therefore, cooler) during the last solar minimum phase (than it had ever been since the beginning of the space age (Solomon et al., 2010)).

5. Conclusions

The effects of solar irradiance variations on atomic oxygen in the MLT region were studied at the 11-year and the 27-day time scales. The analyses were performed on the atomic oxygen concentration time series retrieved on the base of oxygen green line nightglow observations at 557.7 nm wavelength at low latitudes, which were provided by SCIAMACHY onboard Envisat from 01/2003 to 12/2011.

The sensitivity of atomic oxygen to solar forcing was determined for the solar 11-year and 27-day cycles with use of different solar proxies, i.e., the MgII index, Lyman-α irradiance and the F10.7 cm radio flux.

The results on sensitivity of annually averaged atomic oxygen concentration time series to solar forcing are consistent with known experimental and model studies, and exhibit relative variations in oxygen of about 20% in the 90 – 100 km altitude range over the time interval from the end of the solar maximum phase to the end of the solar minimum phase. Two more of our results concerning [O] sensitivity, which deserve further studies, are: (a) good agreement of [O] sensitivities to solar forcing at the 11-year and the 27-day time scales, (b) lower [O] sensitivity values at the 27-day time scale during the last solar minimum phase.

Using cross-correlation and the superposed epoch analysis techniques, a statistically significant solar 27-day signature for the first time has been identified on the base of [O] data sets provided by SCIAMACHY. The time lag between solar forcing and the response of atomic oxygen can reach about 13 days that is about a quarter of the 27-day cycle longer in comparison to the known model results (Gruzdev et al., 2009). The reason of this difference is currently not known, but such a reason is supposed to be found in further studies, provided that both photochemistry and dynamical variability would be taken into account.

The SCIAMACHY [O] response to solar forcing was successfully modeled on the base of the standard multiple-linear regression approach at the 11-year time scale. The components of the used regression equation take into account seasonal, solar and QBO variations as well as a long-term trend. The sensitivity of atomic oxygen to solar forcing quantified with use of this model is in good agreement with the results obtained on the base of the annually averaged values, see Section 4.3.

The sensitivity of atomic oxygen at the 11-year time scale is found to be strongly dependent on altitude, which determines relative 11-year

solar cycle variations of about 5% at about 90 km and about 25% at about 100 km in agreement with known results.

Note that atomic oxygen was retrieved from SCIAMACHY oxygen green line nightglow observations with use of two different photochemical schemes: the well-known cubic equation (McDade et al., 1986) with coefficients as discussed by Lednyts'kyy et al. (2015), and an extended cubic equation (Gobbi et al., 1992; Semenov, 1997) with corresponding coefficients (Lednyts'kyy et al., 2015) to include processes of O(^{1}S) quenching by other chemical species in the MLT. Although there is a difference (about 30%) between the retrieval results of these two photochemical schemes, the sensitivities of atomic oxygen to solar forcing for both photochemical schemes are in good agreement.

Acknowledgements

This work was supported by Ernst-Moritz-Arndt-University of Greifswald and by the Deutsche Forschungsgemeinschaft (DFG) under grant SA 1351. SCIAMACHY is jointly funded by Germany, the Netherlands and Belgium. We are indebted to ESA (European Space Agency) for providing the SCIAMACHY Level 1 data used in this study. The authors thank M. Sinnhuber (Karlsruhe Institute of Technology), Gary Thomas (Laboratory for Atmospheric and Space Physics), Matthew DeLand (Science Systems and Applications, Inc.), the anonymous reviewer #1, the guest editor Xinzhao Chu (University of Colorado Boulder) for helpful discussions and insightful comments and especially the anonymous reviewer #2 for very interesting, helpful comments, recommendations, and suggestions.

References

Angelats i Coll, M., Forbes, J.M., 1998. Dynamical influences on atomic oxygen and 5577 Å emission rates in the lower thermosphere. Geophys. Res. Lett. 25 (4), 461–464. http://dx.doi.org/10.1029/98GL00130.

Baldwin, M.P., Gray, L.J., Dunkerton, T.J., Hamilton, K., Haynes, P.H., Randel, W.J., Holton, J.R., Alexander, M.J., Hirota, I., Horinouchi, T., Jones, D.B.A., Kinnersley, J.S., Marquardt, C., Sato, K., Takahashi, M., 2001. The quasi-biennial oscillation. Rev. Geophys. 39 (2), 179–229. http://dx.doi.org/10.1029/1999RG000073.

Beig, G., Scheer, J., Mlynczak, M.G., Keckhut, P., 2008. Overview of the temperature response in the mesosphere and lower thermosphere to solar activity. Rev. Geophys. 46 (3), RG3002. http://dx.doi.org/10.1029/2007RG000236.

Blarquez, O., Carcaillet, C., 2010. Fire, fuel composition and resilience threshold in subalpine ecosystem. PLoS One 5 (8), e12480. http://dx.doi.org/10.1371/journal.pone.0012480.

Bovensmann, H., Burrows, J.P., Buchwitz, M., Frerick, J., Noël, S., Rozanov, V.V., Chance, K.V., Goede, A.P.H., 1999. SCIAMACHY: mission Objectives and Measurement Modes. J. Atmos. Sci. 56 (2), 127–150. http://dx.doi.org/10.1175/1520-0469(1999)056<0127:SMOAMM>2.0.CO;2.

Brasseur, G.P., Solomon, S., 2005. Aeronomy of the Middle Atmosphere: Chemistry and Physics of the Stratosphere and Mesosphere 3rd edition. Springer, Netherlands, 644. http://dx.doi.org/10.1007/1-4020-3824-0.

Burrage, M.D., Vincent, R.A., Mayr, H.G., Skinner, W.R., Arnold, N.F., Hays, P.B., 1996. Long-term variability in the equatorial middle atmosphere zonal wind. J. Geophys. Res. 101 (D8), 12847–12854. http://dx.doi.org/10.1029/96JD00575.

Chree, C., 1913. Some phenomena of sunspots and of terrestrial magnetism at Kew Observatory. Philos. Trans. R. Soc. Ser. A 212, 75–116. http://dx.doi.org/10.1098/rsta.1913.0003.

Colegrove, F.D., Hanson, W.B., Johnson, F.S., 1965. Eddy diffusion and oxygen transport in the lower thermosphere. J. Geophys. Res. 70 (19), 4931–4941. http://dx.doi.org/10.1029/JZ070i019p04931.

Dudok de Wit, T., Kretzschmar, M., Lilensten, J., Woods, T., 2009. Finding the best proxies for the solar UV irradiance. Geophys. Res. Lett. 36 (10), L10107. http://dx.doi.org/10.1029/2009GL037825.

Dukok de Wit, T., Watermann, J., 2010. Solar forcing of the terrestrial atmosphere. C. R. Geosci. 342 (4–5), 259–272. http://dx.doi.org/10.1016/j.crte.2009.06.001.

Ebisuzaki, W., 1997. A method to estimate the statistical significance of a correlation when the data are serially correlated. J. Clim. 10 (9), 2147–2153. http://dx.doi.org/10.1175/1520-0442(1997)010<2147:AMTETS>2.0.CO;2.

Eckermann, S.D., Rajopadhyaya, D.K., Vincent, R.A., 1997. A selection of papers presented at the iugg xxi general assembly on large-scale structure, dynamics and aeronomy of the upper atmosphere intraseasonal wind variability in the equatorial mesosphere and lower thermosphere: long-term observations from the central pacific. J. Atmos. Sol. -Terr. Phys. 59 (6), 603–627. http://dx.doi.org/10.1016/S1364-6826(96)00143-5.

Fioletov, V.E., 2009. Estimating the 27-day and 11-year solar cycle variations in tropical upper stratospheric ozone. J. Geophys. Res. 114 (D2), 2156–2202. http://dx.doi.org/10.1029/2008JD010499, (D02302).

Gobbi, D., Takahashi, H., Clemesha, B.R., Batista, P.P., 1992. Equatorial atomic oxygen profiles derived from rocket observations of OI 557.7 nm airglow emission. Planet. Space Sci. 40 (6), 775–781. http://dx.doi.org/10.1016/0032-0633(92)90106-X.

Gruzdev, A.N., Schmidt, H., Brasseur, G.P., 2009. The effect of the solar rotational irradiance variation on the middle and upper atmosphere calculated by a three-dimensional chemistry-climate model. Atmos. Chem. Phys. 9 (2), 595–614. http://dx.doi.org/10.5194/acp-9-595-2009.

Hood, L.L., 1986. Coupled stratospheric ozone and temperature responses to short-term changes in solar ultraviolet flux: an analysis of nimbus 7 SBUV and SAMS data. J. Geophys. Res. 91 (D4), 5264–5276. http://dx.doi.org/10.1029/JD091iD04p05264.

Huang, K.M., Liu, A.Z., Zhang, S.D., Yi, F., Huang, C.M., Gan, Q., Gong, Y., Zhang, Y.H., Wang, R., 2015. Observational evidence of quasi-27-day oscillation propagating from the lower atmosphere to the mesosphere over 20 ºN. Ann. Geophys. 33 (10), 1321–1330. http://dx.doi.org/10.5194/angeo-33-1321-2015.

IEPUB: Institute of Environmental Physics, University of Bremen, Composite Mg II Index dataset, available at: ⟨http://www.iup.uni-bremen.de/UVSAT/Datasets/mgii⟩ (accessed 03.07.15).

Isobe, T., Feigelson, E.D., Akritas, M.G., Babu, G.J., 1990. Linear regression in astronomy. Astrophys. J. 364 (20), 104–113. http://dx.doi.org/10.1086/169390.

Kaufmann, M., Zhu, Y., Ern, M., Riese, M., 2014. Global distribution of atomic oxygen in the mesopause region as derived from SCIAMACHY O(^{1}S) green line measurements. Geophys. Res. Lett. 41 (17), 6274–6280. http://dx.doi.org/10.1002/2014GL060574.

Lednyts'kyy, O., von Savigny, C., Eichmann, K.-U., Mlynczak, M.G., 2015. Atomic oxygen retrievals in the MLT region from SCIAMACHY nightglow limb measurements. Atmos. Meas. Tech. 8, 1021–1041. http://dx.doi.org/10.5194/amt-8-1021-2015.

LISIRD: LASP Interactive Solar IRradiance Data Center, composite Lyman-α dataset, available at: ⟨http://lasp.colorado.edu/lisird/lya/⟩ (accessed 03.07.15).

Liu, G., Shepherd, G.G., 2008. An investigation of the solar cycle impact on the lower thermosphere O(^{1}S) nightglow emission as observed by WINDII/UARS. Adv. Space Res. 42 (5), 933–938. http://dx.doi.org/10.1016/j.asr.2007.10.008.

Liu, G., Shepherd, G.G., Roble, R.G., 2008. Seasonal variations of the nighttime O(1S) and OH airglow emission rates at mid-to-high latitudes in the context of the large-scale circulation. J. Geophys. Res. 113 (A6), 2156–2202. http://dx.doi.org/10.1029/2007JA012854.

Luo, Y., Manson, A.H., Meek, C.E., Igarashi, K., Jacobi, Ch., 2001. Extra long period (20–40 day) oscillations in the mesospheric and lower thermospheric winds: observations in Canada, Europe and Japan, and considerations of possible solar influences. J. Atmos. Sol. -Terr. Phys. 63 (9), 835–852. http://dx.doi.org/10.1016/S1364-6826(00)00206-6.

Markwardt, C.B. (2009). Non-linear Least-squares Fitting in IDL with MPFIT. In Bohlender, D. A., Daniel, D., Patrick, D. (Eds.), Astronomical Data Analysis Software and Systems, XVIII, 251 - 254, ASP Conf. Ser., 411 pages.

Marsh, D.R., Garcia, R.R., Kinnison, D.E., Boville, B.A., Sassi, F., Solomon, S.C., Matthes, K., 2007. Modeling the whole atmosphere response to solar cycle changes in radiative and geomagnetic forcing. J. Geophys. Res. 112 (D23), D23306. http://dx.doi.org/10.1029/2006JD008306.

McDade, I.C., Murtagh, D.P., Greer, R.G.H., Dickinson, P.H.G., Witt, G., Stegman, J., Llewellyn, E.J., Thomas, L., Jenkins, D.B., 1986. ETON 2: Quenching parameters for the precursors of $O_2(b^1\Sigma_g^+)$ and O(^{1}S) in the terrestrial nightglow. Planet. Space Sci. 34, 789–800. http://dx.doi.org/10.1016/0032-0633(86)90075-9.

McIntosh, S.W., Wang, X., Leamon, R.J., Howe, R., Krista, L.D., Malanushenko, A.V., Cirtain, J.W., Gurman, J.B., Pesnell, W.D., Thompson, M.J., 2014. Deciphering solar magnetic activity I: on the relationship between the sunspot cycle and the evolution of small magnetic features. Astrophys. J. 792 (1), 1–36. http://dx.doi.org/10.1088/0004-/792/1/12.

McIntosh, S.W., Leamon, R.J., Krista, L.D., Title, A.M., Hudson, H.S., Riley, P., Harder, J.W., Kopp, G., Snow, M., Woods, T.N., Kasper, J.C., Stevens, M.L., Ulrich, R.K., 2015. The solar magnetic activity band interaction and instabilities that shape quasi-periodic variability. Nat. Commun. 6 (6491), 1–11. http://dx.doi.org/10.1088/0004-637X/792/1/12.

McLandress, C., Shepherd, G.G., Solheim, B.H., 1996. Satellite observations of thermospheric tides: results from the wind imaging interferometer on UARS. J. Geophys. Res. 101 (D2), 4093–4114. http://dx.doi.org/10.1029/95JD03359.

NOAA: National Geophysical Data Center, Kp and Ap datasets, available at: ftp://ftp.ngdc.noaa.gov/STP/GEOMAGNETIC_DATA/INDICES/KP_AP/ (accessed 03.07.15).

Pancheva, D., 2001. Non-linear interaction of tides and planetary waves in the mesosphere and lower thermosphere: observations over Europe. Phys. Chem. Earth C 26 (6), 411–418. http://dx.doi.org/10.1016/S1464-1917(01)00022-8.

Pancheva, D., Mitchell, N., Middleton, H., Muller, H., 2003. Variability of the semidiurnal tide due to fluctuations in solar activity and total ozone. J. Atmos. Sol. -Terr. Phys. 65 (1), 1–19. http://dx.doi.org/10.1016/S1364-6826(02)00084-6.

Press, W.H., Teukolsky, S.A., Vetterling, W.T., Flannery, B.P., 1997. Numerical Recipes in Fortran 77, The Art of Scientific Computing Vol. 1, 2ed., Cambridge University Press, 1574, ISBN: 0-521-43064-X.

Robert, C.E., von Savigny, C., Rahpoe, N., Bovensmann, H., Burrows, J.P., DeLand, M.T., Schwartz, M.J., 2010. First evidence of a 27 day solar signature in noctilucent cloud occurrence frequency. J. Geophys. Res. 115 (D1), D00I12. http://dx.doi.org/10.1029/2009JD012359.

Rottman, G.J., 1988. Observations of solar UV and EUV variability. Adv. Space Res. 8 (7), 53–66. http://dx.doi.org/10.1016/0273-1177(88)90172-X.

Russell, J.P., Lowe, R.P., Ward, W.E., 2004. Atomic oxygen annual and semi-annual variations in the mesopause region for mid and equatorial latitudes. J. Atmos. Sol. -Terr. Phys. 66 (6–9), 451–461. http://dx.doi.org/10.1016/j.jastp.2004.01.004.

Schmidt, H., Brasseur, G.P., Charron, M., Manzini, E., Giorgetta, M.A., Diehl, T.,

Fomichev, V.I., Kinnison, D., Marsh, D., Walters, S., 2006. The HAMMONIA chemistry climate model: sensitivity of the mesopause region to the 11-year solar cycle and CO_2 doubling. J. Atmos. Sci. 19, 3903–3931. http://dx.doi.org/10.1175/JCLI3829.1.

Semenov, A.I., 1997. Long-term changes in the height profiles of ozone and atomic oxygen in the lower thermosphere. Geomagn. Aeronomy. 37 (3), 354–360.

Snow, M., Weber, M., Machol, J., Viereck, R., Richard, E., 2014. Comparison of magnesium ii core-to-wing ratio observations during solar minimum 23/24. J. Space Weather Space Clim. 4 (A04), 1–6. http://dx.doi.org/10.1051/swsc/2014001.

Solomon, S.C., Woods, T.N., Didkovsky, L.V., Emmert, J.T., Qian, L., 2010. Anomalously low solar extreme-ultraviolet irradiance and thermospheric density during solar minimum. Geophys. Res. Lett. 37 (16), L16103. http://dx.doi.org/10.1029/2010GL044468.

Tapping, K.F., 2013. The 10.7 cm solar radio flux (F10.7). Space Weather 11 (7), 394–406. http://dx.doi.org/10.1002/swe.20064.

Teiser, G., von Savigny, C., 2016. Variability of OH(3-1) and OH(6-2) emission altitude and volume emission rate from 2003 to 2011, submitted to J. Atm. Sol.-Terr. Phys., this issue.

Thomas, G.E., Thurairajah, B., Hervig, M.E., von Savigny, C., Snow, M., 2015. Solar-induced 27-day variations of mesospheric temperature and water vapor from the AIM SOFIE experiment: drivers of polar mesospheric cloud variability. J. Atmos. Sol.-Terr. Phys. 134, 56–68. http://dx.doi.org/10.1016/j.jastp.2015.09.015.

Torrence, C., Webster, P.J., 1999. Interdecadal changes in the ENSO-monsoon system. J. Clim. 12, 2679–2690. http://dx.doi.org/10.1175/1520-0442(1999)012<2679:ICITEM>2.0.CO;2.

von Savigny, C., Eichmann, K.-U., Llewellyn, E.J., Bovensmann, H., Burrows, J.P., Bittner, M., Höppner, K., Offermann, D., Taylor, M.J., Zhao, Y., Steinbrecht, W., Winkler, P., 2004. First near-global retrievals of OH rotational temperatures from satellite-based Meinel band emission measurements. Geophys. Res. Lett. 31 (15), L15111. http://dx.doi.org/10.1007/978-94-007-4348-9.

von Savigny, C., Eichmann, K.-U., Robert, C.E., Burrows, J.P., Weber, M., 2012. Sensitivity of equatorial mesopause temperatures to the 27-day solar cycle. Geophys. Res. Lett. 39 (21), L21804. http://dx.doi.org/10.1029/2012GL053563.

von Savigny, C., Lednyts'kyy, O., 2013. On the relationship between atomic oxygen and vertical shifts between OH Meinel bands originating from different vibrational levels. Geophys. Res. Lett. 40 (21), 5821–5825. http://dx.doi.org/10.1002/2013GL058017.

von Savigny, C., Lednyts'kyy, O., Forbes, J.M., Zhang, X., 2015. Lunar semidiurnal tide in the terrestrial airglow. Geophys. Res. Lett. 42 (9), 3553–3559. http://dx.doi.org/10.1002/2015GL063567.

von Savigny, C., Robert, C., Rahpoe, N., Winkler, H., Becker, E., Bovensmann, H., Burrows, J.P., DeLand, M.T., 2013. Impact of short term solar variability on the polar summer mesopause and noctilucent clouds, Chapter 20 In: Climate and Weather of the Sun-Earth-System (CAWSES): Highlights from a priority program, Springer Atmospheric Sciences, 365 – 382, Springer, Dordrecht, The Netherlands, ISBN: 978-94-007-4347-2, 634 pages, http://dx.doi.org/10.1007/978-007-9.

Ward, W.E., 1999. A simple model of diurnal variations in the mesospheric oxygen nightglow. Geophys. Res. Lett. 26 (23), 3565–3568. http://dx.doi.org/10.1029/1999GL003661.

Weber, M., Pagaran, J., Dikty, S., von Savigny, C., Burrows, J.P., DeLand, M., Floyd, L.E., Harder, J.W., Mlynczak, M.G., Schmidt, H., 2013. Investigation of solar irradiance variations and their impact on middle atmospheric ozone, Chapter 3 In Lübken, F.-J. (Ed.), Climate And Weather of the Sun-Earth System (CAWSES): Highlights from a priority program, 39 – 54, Springer, Dordrecht, The Netherlands, ISBN: 978-94-007-4347-2, 634 pages, http://dx.doi.org/10.1007/978-94-007-4348-9.

Woods, T.N., Tobiska, W.K., Rottman, G.J., Worden, J.R., 2000. Improved solar lyman-α irradiance modeling from 1947 through 1999 based on UARS observations. J. Geophys. Res. 105 (A12), 27195–27215. http://dx.doi.org/10.1029/2000JA000051.

Zechmeister, M., Kürster, M., 2009. The generalised Lomb-Scargle periodogram. a new formalism for the floating-mean and keplerian periodograms. Astron. Astrophys. 496 (2), 577–584. http://dx.doi.org/10.1051/0004-6361:200811296.

Zhu, Y., Kaufmann, M., Ern, M., Riese, M., 2015. Nighttime atomic oxygen in the mesopause region retrieved from SCIAMACHY O(1S) green line measurements and its response to solar cycle variation. J. Geophys. Res. Space Phys. 120 (10), 9057–9073. http://dx.doi.org/10.1002/2015JA021405.